SIMULATING THE UNSTEADY HYDRODYNAMICS OF A ROWING OAR BLADE

SIMULATING THE UNSTEADY HYDRODYNAMICS OF A ROWING OAR BLADE DURING A STROKE

By

ANDREW SLIASAS, B.ENG. MANAGEMENT

A Thesis

Submitted to the School of Graduate Studies

In Partial Fulfillment of the Requirements

For the Degree

Masters of Applied Science

McMaster University

© Copyright by Andrew Sliasas, September 2009

MASTERS OF APPLIED SCIENCE (2009) McMaster University

(Mechanical Engineering) Hamilton, Ontario

TITLE:	Simulating the unsteady hydrodynamics of a rowing oar blade during a stroke
AUTHOR:	Andrew Sliasas, B.Eng. Management (McMaster University)
SUPERVISOR:	Stephen Tullis, Ph.D.
NUMBER OF PAGES:	xvi, 78

ABSTRACT

The highly unsteady free surface flow around a rowing oar blade in motion is investigated using modelling techniques. The ability of the numerical model to replicate this complex flow is demonstrated by using computational fluid dynamics (CFD) to simulate previously performed steady-state experiments involving a quarter-scale rowing blade in a water flume. A comparison of drag and lift coefficients from the experiments and the simulations reveals excellent agreement, providing confidence in the numerical model to handle similar flow conditions. The computational domain is then expanded to simulate a full-scale blade in open water conditions, and steady-state drag and lift coefficients are compared to those previously simulated for a quarter-scale blade in a flume, revealing substantial differences in magnitude. The computational domain is then modified to allow for oar rotation, as in actual rowing. A force-based rowing model is derived, calculating the instantaneous velocity of a shell based on the propulsive force generated by the motion of the oar blade in the water, the hydrodynamic drag on the shell, and the motion of the rowers within the shell. Using the shell velocity and a prescribed oar angular velocity, the CFD model calculates the highly unsteady blade flow, providing instantaneous drag, lift, and propulsive forces on the blade, in turn driving the rowing model.

The dynamic blade-water interaction is depicted in six distinct flow regimes, characterized by the relative motion of the blade in the water and the temporal influence of drag and lift. It is seen that the propulsive force generated by the blade is largely lift-induced through the first half of the stroke. During the middle of the stroke, drag increasingly influences the propulsive force. At end of the stroke, the propulsive force is once again largely lift-induced.

ACKNOWLEDGEMENTS

For the inspiration and guidance, and for the opportunity,

I would like to thank Dr. Stephen Tullis

To curiosity,

to going with a feeling,

to finding a poster taped to a wall and changing your life

Table of Contents

List of Figures

List of Tables

List of Symbols

A_{proj}: oar blade projected area

A_{shell}: shell wetted area

$a_{relative,crew}$: crew acceleration relative to the shell

a_{shell}: shell acceleration

C_D: drag coefficient

C_L: lift coefficient

$CD_{k\omega}$: cross-diffusion term limiter

c: nondimensional skin friction drag coefficient

F_1: blending function

F_2: blending function

F_{drag}: oar blade drag force

$F_{drag,shell}$: shell drag force

F_{lift}: oar blade lift force

$F_{momentum,crew}$: momentum of the crew motion relative to the shell

$F_{net,blade}$: net blade force

$F_{net,shell}$: net shell force

$F_{propulsive}$: propulsive force from one oar blade

$F_{propulsive,crew}$: net propulsive force from all oar blades

g_j: acceleration due to gravity

I: turbulence intensity

k: turbulent kinetic energy

k_{drag}: drag factor

m_{crew}: crew mass

m_{shell}: shell mass

m_{total}: combined mass of crew and shell

n_{oars}: number of oars

P: mean pressure

P_k: production of turbulence limiter

p: instantaneous pressure

p': pressure fluctuation

Re: Reynolds number

S: strain rate

$S_{centrifugal}$: centrifugal force source term

$S_{Coriolis}$: Coriolis force source term

S_{Euler}: Euler force source term

S_M: momentum source term

S_{shell}: shell velocity source term

t: time

U_i: mean velocity component in the x-direction

u_i: instantaneous velocity component in the x-direction

u_i': fluctuating velocity component in the x-direction

v_{blade}: linear velocity of the blade chord centre

v_{flume}: water flume velocity

$v_{relative}$: incident flow velocity at the blade chord centre

$v_{relative,crew}$: crew velocity relative to the shell

v_{shell}: shell velocity

x_i: Cartesian x-coordinate

y: distance to the wall

α: angle of attack

$\alpha_{nominal}$: angle of attack at blade chord centre

ε: turbulence dissipation rate

θ_{oar}: angle of oar shaft relative to the shell centre-line

μ: dynamic viscosity

μ_t: turbulent viscosity

ν: kinematic viscosity

ρ: fluid density

φ: fluid volume fraction

ω: turbulence frequency

ω_{oar}: oar angular velocity

1 Introduction and Literature Review

One particular area of rowing research that has received scant scientific attention to date is the complex hydrodynamics of the oar blade in the water during a stroke. With the emergence of computational fluid dynamics tools to study such complex flows and the required computing power to do so, a complete numerical simulation of oar blade hydrodynamics is now possible. From this knowledge can be wrought numerous benefits – ranging from improved blade shape design to more efficient stroke biomechanics; ultimately leading to faster rowers.

1.1 Rowing equipment

In the competitive sport of rowing, the rower sits in a long, slender boat (the *shell*) and propels him/herself using oars. The number of rowers in a shell (the *crew*) ranges from one to eight, with each rower using either one oar (*sweeping*) or two oars (*sculling*).

Shells vary in length from 10 m for a single scull to 20 m for an eight-oared shell. At the widest point, shell widths range from 30 cm for a single scull to 60 cm for an eight-oared shell. Modern composite shells are also extremely lightweight, with a single shell weighing as little as 14 kg. The rower sits on a sliding seat and faces the stern, with their feet secured to the hull. Extending out from both sides of the shell are *outriggers*, which feature a pivoting *oarlock* to provide transverse restraint for the oar. Contact between the oarlock and a *collar* on the oar also prevents the oar from sliding outboard. The connection between a rower and the oar occurs at the handle. The distance from the end of the handle to the collar is known as the *inboard* length of the oar, and is generally 0.88 m for sculling oars and 1.15 m for sweep oars. The distance from the collar to the blade tip is similarly known as the *outboard*, and this length is approximately 2.0 m for sculling oars and 2.6 m for sweep oars. The ratio of the outboard to the inboard is known as the *gearing* ratio.

1.2 Equipment design progress

The manufacture of rowing equipment has evolved through the years thanks to advances in materials and fabrication processes. Composite materials have allowed for lighter, stronger, and ultimately more durable equipment. The use of these materials has also afforded rowing equipment companies more freedom in their designs. Oar manufacturers in particular have benefitted from the use of composite materials, allowing for the design and construction of complex blade profiles.

Prior to the early 1990s, the most popular profile shape was the *Macon* blade. It featured a low aspect ratio symmetric face design, and curvature along the blade spine (Figure 1.1). This shape remained the standard profile until the early 1990's when a new, unsymmetrical blade design emerged. Named the *hatchet* (Figure 1.1), this blade shape gained nearly universal acceptance almost immediately after its introduction and continues to be the shape of choice for most oar manufacturers.

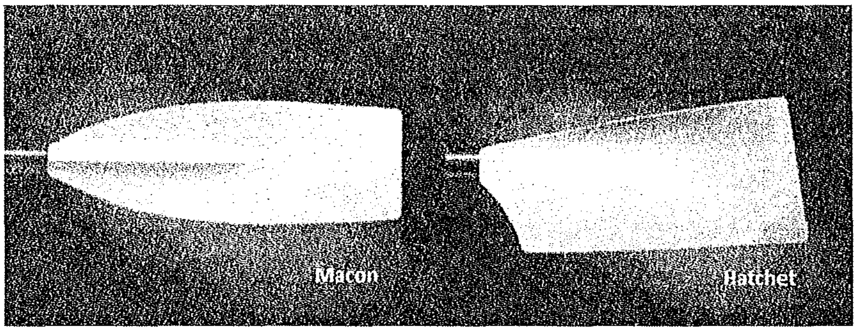

Figure 1.1: Front profile of two popular blade shapes; the Macon on the left and the hatchet on the right (Adapted from Concept2, 2008)

For all of the blade design changes through the years, however, there has been no significant fluid dynamic investigation performed on a blade under actual rowing conditions. All design innovations to date have been based and tested on a qualitative assessment of what would constitute an effective blade shape (Concept2, 2007). The potential for blade design improvements stemming from a greater knowledge of blade hydrodynamics, then, should be considered great, as noted in many rowing studies (Wellicome, 1967; Pope, 1973; Millward, 1987; Baudouin & Hawkins, 2002; Caplan & Gardner, 2007a; Atkinson, 2007; Macrossan, 2008; Nolte, 2009).

1.3 The rowing stroke

The complete rowing stroke is comprised of two phases – the *drive* and the *recovery*. At the beginning of the drive (the *catch*), the propulsive portion of the stroke, the rower sits with legs bent and arms outstretched while leaning forward. The oar blade is inserted in the water as the rower accelerates toward the bow, prying the shell forward by extending the legs, leaning back, and drawing the arms into the body in a sequential yet fluid motion (Figure 1.2). Throughout the stroke, the top edge of the blade remains buried slightly below the surface of the water. Observed from a stationary perspective with respect to the water, the oar blade remains locked in a pocket of water throughout the drive, acting as an axis for the shell to lever about. At the end of the drive (the *finish*), the oar is removed from the water and the rower slides back toward the stern, moving into position for the next stroke as the shell glides forward.

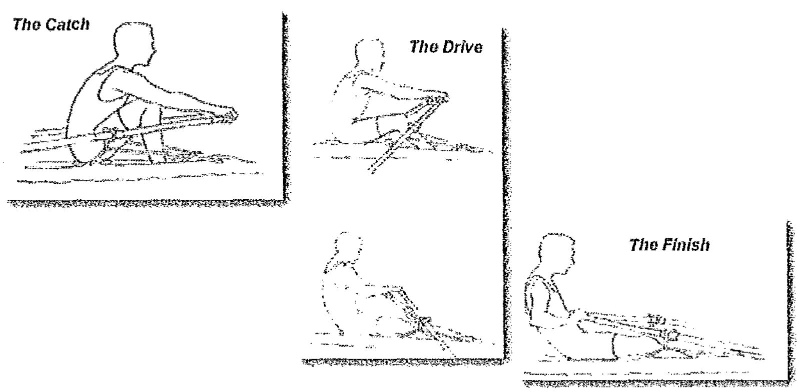

Figure 1.2: Rowing stroke motion (Adapted from History of Collegiate Crew in Connecticut, 2002)

A closer look at the motion of the blade in the water during the drive indicates that it in fact moves within this pocket of water, both parallel and lateral to the shell motion. The nature of this blade motion with respect to the water determines the propulsive force generated by the oar, but to date remains largely unknown.

1.4 Rowing oar blade hydrodynamics research and theory

It was long believed that the resultant force of the water on a rowing blade acts at 90° to its chord line throughout the duration of the stroke. This would mean that near the catch and the finish, when the blade chord is oriented away from orthogonal to the direction of shell motion, only a portion of the blade force contributes to propulsion, while the rest of the force acts perpendicular to the shell motion. Wellicome (1967) was one of the first to view the blade-water interaction from a hydrodynamic perspective. He observed that behind (trailing) the blade during a stroke are both an air-filled cavity and an interacting vortex system. The nature of these flow conditions are continually changing, altering the direction of the resultant blade force away from perpendicular to the blade chord line, particularly near the catch and finish. The result is that near the catch and the finish the blade force is directed more in line with the shell velocity than previously assumed, meaning that these areas of the stroke also contribute significantly to propulsion. Nolte (1993) argued that these favourably aligned forces near the catch and the finish are attributed to lift effects on the blade. He believed that a shallow flow angle of attack on the blade causes the blade to behave like a hydrofoil, generating a lift force perpendicular to the flow direction. In the absence of relevant data, however, the effect of these theories could not be quantified.

The primary reason for a lack of quantitative oar blade hydrodynamic data lies in the difficulty in obtaining it. An experimental apparatus that can replicate the blade motion through the water caused by an accelerating shell is very difficult to create (Barre & Kobus, 1998). Combined with the challenge of acquiring data pertaining to the flow about the blade from such experiments and the time-intensive process of creating the test equipment, this method of flow study has not been fruitful. Experiments performed under actual rowing conditions have, however, been able to successfully extract certain quantitative data. By fitting rowing equipment with sensors, such setups have been able to record the force applied at the oar handle, the angular position of the oar with respect to the shell, and the velocity of the shell during the stroke (Kleshnev, 1999). The problem with this experimental method is that it is highly unrepeatable, as each individual stroke is strongly dependent on externalities (the rower, water conditions, etc.) As well, the inclusion of sensors and instrumentation alters the delicate balance of the shell. What can be gained confidently from these experiments, however, is how the velocity of the shell and the rotation of the oar are related through a stroke.

Combining the linear motion of the shell, v_{shell}, with the angular velocity of the oar, ω_{oar}, there is a relative flow incident on the blade, $v_{relative}$ (Figure 1.3). The nominal angle of attack on the blade, $\alpha_{nominal}$, is the angle of incidence of $v_{relative}$ on the midpoint of the blade chord line. Although the true angle of attack varies along the length of the chord due to the oar rotation, the use of $\alpha_{nominal}$ is useful in defining a reference for the relative flow on the blade. Acting in line with this relative flow is a drag force on the blade, F_{drag}, and acting perpendicular is a lift force, F_{lift}. The net resultant force on the blade, $F_{net,blade}$, is the vector sum of the drag and lift forces.

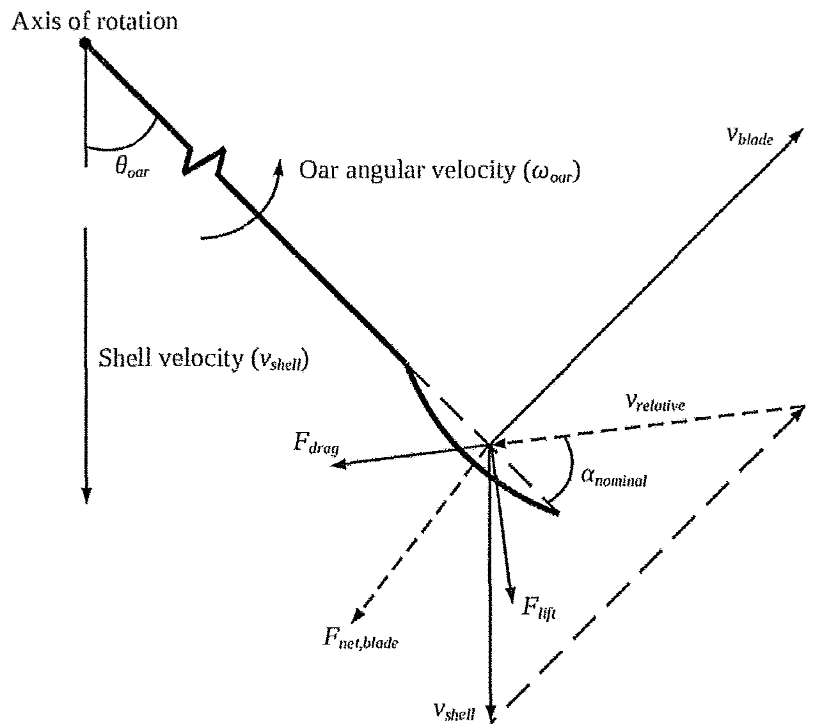

Figure 1.3: Overhead view of a rotating rowing oar during a stroke. The shell is moving downward and the oar is rotating counter-clockwise, resulting in a relative flow on the blade. The oar is shown near the catch, and θ_{oar} ranges from ~ 45° to ~ 135° during the drive. The net force on the blade, broken into drag and lift components, is indicated

As a starting point in understanding the nature of the flow about the blade during the stroke, it is beneficial to look at its path traced through the water from a stationary frame of reference with respect to the water. From his experiments, Kleshnev (1999) observed that when viewed from above, the centre of the blade chord line moves in a *figure-9* pattern through the water during the drive (Figure 1.4). The shell is moving from left to right, with the blade beginning at the bottom left at the catch. Through the stroke the blade moves simultaneously both parallel and lateral to the motion of the shell. The movement of the blade parallel to the motion of the shell is known as *slip*. Positive slip is defined as motion in the same direction as the shell velocity, whereas negative slip is opposite the shell velocity. The lateral motion of the blade is due to the sweep of the oar; the blade moves away from the shell at the beginning of the drive, its motion becoming parallel to the direction of the shell motion, then moves back towards the shell near the end of the drive.

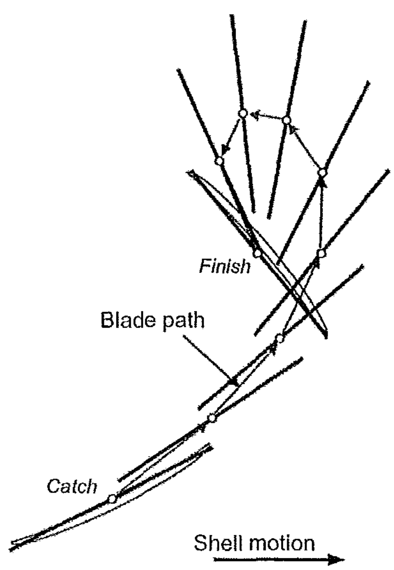

Figure 1.4: From a stationary perspective, an overhead view of the approximate path of the centre of the blade chord line through the water during a stroke. The shell is moving from left to right (adapted with permission from Kleshnev, 1999)

Through the early portion of the drive, the relative flow approaches the blade tip with a very shallow nominal angle of attack of (approximately 0°). During the short time that the blade is in the water during the drive (< 0.75 s), the flow sweeps an arc of approximately 190° across the surface, eventually becoming incident on the back (convex surface) of the blade. This highly transient incident flow combined with the constantly evolving water surface near the blade makes understanding the dynamic three-dimensional flow behaviour quite difficult, and is why it remains for the most part unknown.

While the primary goal of this thesis is to employ computational fluid dynamics to investigate in detail the flow associated with a blade in motion, a model must also be created that is able to replicate the conditions of a rowing stroke. Although numerous rowing models that attempt to simulate shell velocity based on a specified input exist, each lacks in their simplistic treatment of the propulsive force generated by the blade in the water.

1.5 Previous rowing models

It should be noted that a rowing model can at best be employed as a predictor of relative results. Outcomes of elite level 2000 m rowing races are often decided by only several metres (differences on the order of 0.1%). Influences external to the equipment (the rowers, water conditions, etc.) certainly impact heavily on race outcomes. The relative speed advantage that can be obtained with an isolated change in equipment, however, with other factors held constant, can be measured using an appropriate model.

The majority of rowing models are analytical in nature, attempting to simulate the velocity of a shell by simplifying the forces involved. One such model proposed by Millward (1987) is based on a force balance on the shell, where the force generated by the oars is opposed by a drag force on the shell. It was assumed that the oar rotates about a stationary vertical axis located through the centre of the blade, which remains fixed in the water through the drive. The force applied at the oar handle, then, is fully transmitted to the water through the blade. This simplification is analogous to perfect efficiency in transferring power from the rower to the water, neglecting any hydrodynamic characteristics of the blade. Millward also treated the rowers as stationary with respect to the shell, neglecting the effect of their motion on the momentum of the shell. A model by Brearley, de Mestre, and Watson (1998) was similar to the Millward model, except that it also accounted for the momentum of the rowers' motion within the shell. This model still contained the limiting behaviour of the blade acting as a fixed vertical axis in the water, however.

A rowing model by Pope (1973), also based upon force balances on the shell and the crew, sought to determine the shell velocity during a stroke by accounting for hydrodynamic characteristics of the oar blade. Pope hypothesized that only the component of the relative flow incident normal to the blade chord line was responsible for the generated blade force. That is, he assumed that the blade only experiences drag as it moves through the water. The direction of the resultant blade force, then, always acts perpendicular to the blade chord throughout the stroke. The magnitude of this blade force was proportional to the square of the relative blade flow velocity and was calculated, in the absence of more appropriate data, using drag coefficients for a surface-piercing flat plate. Although the rowing model by Pope was the first to consider hydrodynamic effects on a blade in motion, by not incorporating lift it did not capture the full flow behaviour.

As mentioned earlier, the angle of the incident flow on the blade sweeps across the surface throughout the stroke, leading to varying influences of drag and lift. In addition, the top edge of the blade is held just below the water during the stroke, causing surface deformation. The drag and lift coefficients for a blade held stationary near the water surface over a range of angles of attack was investigated by Caplan and Gardner (2007b). In their experiments, a curved rectangular plate with the same curvature and projected surface area as a quarter-scale hatchet blade was held fixed in a flume as water was forced past. Sensors on the oar shaft were used to resolve the force of the water on the blade, which allowed drag and lift coefficients to be calculated. Caplan and Gardner (2007a) also designed a force-based analytical rowing model that was driven by a prescribed oar angular velocity. This model differed from previous rowing models in that it included of both drag and lift forces on the blade. By using the instantaneous shell velocity and oar angular position and velocity to determine the angle of attack of the flow, and applying the corresponding drag and lift coefficients from their stationary blade experiments, a resultant blade force was calculated. Applying a similar force balance on the rowers and the shell as in previous models, a shell velocity profile during a stroke was obtained. A study by Macrossan (2008), however, noted that the drag and lift characteristics for a stationary oar blade are likely significantly different than that for a blade in motion. Although they did not test this, they stated that since the incident blade flow sweeps an arc of nearly 190° in less than one second, it seems hardly likely that the flow can be characterized using steady-state drag and lift coefficients, as in Caplan and Gardner (2007a).

1.6 Unsteady blade flow characteristics

The effect that a quickly changing angle of attack has on the flow behaviour of a blade in motion can be drawn from experiments on pitching airfoils. Flow visualization experiments on rapidly pitching airfoils show that for cases where the angle of attack is increasing from 0°, the airfoil motion changes drag and lift characteristics from what is seen at steady-state (eg. McCroskey, 1982). The pitching motion of an airfoil tends to create a vortex roll-up as the flow moves past the leading edge. These vortices are eventually shed in the airfoil wake, which affects the absolute pressure near its trailing edge, resulting in the airfoil effectively experiencing a shallower angle of attack. As a result, the streamlines over a pitching airfoil remain attached at values of α which would normally cause flow separation for a stationary airfoil, resulting in maximum drag and lift coefficients for a pitching airfoil which exceed those under static conditions. These behaviours further suggest that the steady-state drag and lift coefficients for a rowing blade will differ from those when a blade is in motion.

1.7 Objectives and motivation

The primary objective of this thesis is to investigate the three-dimensional, highly unsteady free surface flow around a rowing blade in motion during a stroke. Several intermediate steps are required, however, in order to achieve this. Chapter 2 begins with an outline of the quarter-scale blade in a water flume experiments performed by Caplan and Gardner (2007b). A detailed description of the flow simulation reproducing these steady-state experiments follows, including a brief literature review of the numerical modelling techniques employed (free surface modelling, turbulence modelling) and an outline of the CFD model. A comparison of the results obtained from the flow simulation with the experimental results (Caplan & Gardner, 2007b) allow validation of the numerical model. The modelled blade is then enlarged to full-scale and steady-state flow characteristics in open water conditions are compared to those at quarter-scale in the flume. Chapter 3 begins by outlining the development of a hydrodynamic-based analytical rowing model, simulating the resultant shell velocity based on the conditions of a stroke. The CFD domain model is then modified to allow for blade rotation, and rotational terms are added to the numerical code to account for the flow in the new domain. The ability of the rowing model to replicate the hydrodynamic conditions of a rowing stroke is validated by comparing the resultant shell velocity to experimental data.

A detailed hydrodynamic examination of the unsteady blade-water interaction during the drive follows, where six distinct flow phases occurring during the drive are outlined, and their impact on the motion of the shell are discussed. Concluding remarks and the direction of future work are outlined in Chapter 4.

2 Steady-State Analyses

2.1 Quarter-scale blade in flume experiments (Caplan & Gardner, 2007b)

Experiments performed by Caplan and Gardner (2007b), as mentioned earlier, were carried out to determine the drag and lift coefficients for a stationary rowing oar blade. In their experiments a curved rectangular plate with a projected surface area of 77.5 cm^2, representing a quarter-scale oar blade, was held fixed in a water flume having a width of 64 cm and depth of 15 cm. The top edge of the blade was flush with the surface of the water and the free-stream water velocity of the flume was 0.75 m/s. Normal and tangential blade forces were measured using strain gauges located on the shaft holding the blade. The forces were recorded over 15 s, with a sampling frequency of 2.5 kHz, and then averaged over the period. Four trials of 15 s were performed for each blade angle, and the mean blade normal and tangential forces over the four trials were calculated. These forces were then decomposed into drag and lift force components, which were then used to calculate drag and lift coefficients. These steady-state experiments were run with the blade held at α values ranging from 0° to 180° in 5° increments.

2.2 Quarter-scale blade in water flume simulations

The first step towards simulating unsteady oar blade hydrodynamics was to validate the ability of the computational fluid dynamic (CFD) model to handle similar three-dimensional free surface flow conditions. This validation was accomplished by modelling the steady-state oar blade experiments of Caplan and Gardner (2007b), then comparing the calculated drag and lift coefficients to the experimental values.

2.2.1 Numerics

Simulating the flow around an oar blade was achieved by numerically solving the governing equations for the fluid motion, adjusted to model a finite free surface interface between the water and air phases and to account for the turbulent characteristics of the flow. These coupled, highly nonlinear equations are calculated for the flow using a finite volume approach, where the fluid domain is divided into a finite number of three-dimensional grid elements (control volumes), and the governing equations are applied at each of these elements.

2.2.1.1 Navier-Stokes equations

The governing equations defining fluid flow are comprised of the conservation of mass (continuity) equations and the conservation of momentum equations, and are collectively known as the Navier-Stokes equations. For a single-phase flow, the general form of the mass and momentum equations are, respectively,

$$\frac{\partial \rho}{\partial t}+\frac{\partial}{\partial x_i}(\rho u_i)=0 \tag{2.1}$$

$$\frac{\partial}{\partial t}(\rho u_j)+\frac{\partial}{\partial x_i}(\rho u_i u_j)=-\frac{\partial p}{\partial x_j}+\frac{\partial}{\partial x_i}\left[\mu\left(\frac{\partial u_j}{\partial x_i}+\frac{\partial u_i}{\partial x_j}\right)\right]-\rho g_j \tag{2.2}$$

In order to account for the free surface distinction between the air and water phases, and to accommodate turbulence quantities in the flow, these equations need to be appropriately modified.

2.2.1.2 Numerical modelling of free surfaces

The free surface distinction between the water and air phases is accomplished using a volume of fluid (*VOF*) multiphase flow method (Hirt & Nichols, 1981). This is based on a Eulerian treatment of the flow, where the domain grid structure remains fixed as the motion of the fluid through it is calculated. In addition, all fluid phases within the domain are treated as a single continuum flow field, sharing common transported velocity and pressure quantities. The volume fraction of each fluid, φ, within each domain grid element is tracked during the solution stage. Most elements contain either entirely water ($\varphi_{water} = 1$) or entirely air ($\varphi_{air} = 1$). Elements along the interface between the water and air take on a fractional φ value ($0 < \varphi < 1$). At a given instance, the location of the free surface can be constructed by combining elements of fractional φ in a piecewise manner.

This method accurately tracks the continuous motion of a free surface, accounting for fluid breakup and reattachment (Gueyffier *et al.*, 1999).

2.2.1.3 Multiphase flow equations

The Navier-Stokes equations for a two-phase flow are similar to those for single-phase flow (Equations (2.1) and (2.2)), but incorporate the individual density and dynamic viscosity values of each fluid phase. Assuming volume conservation within each domain element,

$$\varphi_{water} + \varphi_{air} \equiv 1 \tag{2.3}$$

and a homogeneous flow where the transported velocity and pressure quantities are the same across each fluid phase, the conservation of mass equations for the water and air phases are, respectively,

$$\frac{\partial}{\partial t}(\varphi_{water}\rho_{water}) + \frac{\partial}{\partial x_i}(\varphi_{water}\rho_{water}u_i) = 0 \tag{2.4}$$

$$\frac{\partial}{\partial t}(\varphi_{air}\rho_{air}) + \frac{\partial}{\partial x_i}(\varphi_{air}\rho_{air}u_i) = 0 \tag{2.5}$$

The conservation of momentum equations are defined as before,

$$\frac{\partial}{\partial t}(\rho u_j) + \frac{\partial}{\partial x_i}(\rho u_i u_j) = -\frac{\partial p}{\partial x_j} + \frac{\partial}{\partial x_i}\left[\mu\left(\frac{\partial u_j}{\partial x_i} + \frac{\partial u_i}{\partial x_j}\right)\right] - \rho g_j \tag{2.6}$$

although now, density and dynamic viscosity are volume averages of the properties of the fluid phases,

$$\rho = \varphi_{water}\rho_{water} + \varphi_{air}\rho_{air} \tag{2.7}$$

$$\mu = \varphi_{water}\mu_{water} + \varphi_{air}\mu_{air} \tag{2.8}$$

In order to maintain a distinct boundary between the air and water phases, a surface tension force is applied at the free surface. This surface tension force is modelled as a volume force concentrated at the interface, acting to minimize its surface area, thereby providing a smoothed free surface (Brackbill, Kothe, & Zemach, 1992).

Using this free surface multiphase flow model, as implemented in ANSYS CFX, Zwart *et al.* (2008) were able to simulate the wave pattern generated by a moving ship hull, with results agreeing very well with experimental data. The simulation was also able to predict the drag resistance of a hull within 3% of experimental values. The ability of this model to accurately simulate surface waves provides confidence in its use to replicate the free surface deformation around a rowing blade.

2.2.1.4 Turbulence modelling

Most flows of practical interest, the present case included, are turbulent in nature. Incorporating this turbulent behaviour in the conservation equations is achieved by modifying the velocity and pressure quantities to reflect their fluctuating behaviour.

Within a turbulent flow, the instantaneous velocity at a given point (u_i) is defined by a time-averaged mean velocity component (U_i) and a fluctuating velocity component (u_i'),

$$u_i = U_i + u_i' \tag{2.9}$$

The instantaneous pressure field can be similarly written,

$$p = P + p' \tag{2.10}$$

Substituting Equations (2.9) and (2.10) into the two-phase continuity equations, (Equations (2.4) & (2.5)), the time-averaged two-phase continuity equations become,

$$\frac{\partial}{\partial t}(\varphi_{water}\rho_{water}) + \frac{\partial}{\partial x_i}(\varphi_{water}\rho_{water}U_i) = 0 \tag{2.11}$$

$$\frac{\partial}{\partial t}(\varphi_{air}\rho_{air}) + \frac{\partial}{\partial x_i}(\varphi_{air}\rho_{air}U_i) = 0 \tag{2.12}$$

and into the conservation of momentum equations, (Equation (2.6)), the time-averaged two-phase momentum equations become,

$$\frac{\partial}{\partial t}(\rho U_j) + \frac{\partial}{\partial x_i}(\rho U_i U_j) = -\frac{\partial P}{\partial x_j} + \frac{\partial}{\partial x_i}\left[\mu\left(\frac{\partial U_j}{\partial x_i} + \frac{\partial U_i}{\partial x_j}\right) - \rho\overline{u'_j u'_i}\right] - \rho g_j \tag{2.13}$$

Equations (2.11) – (2.13) are also known as the Reynolds Averaged Navier-Stokes (RANS) equations for multiphase flow, and are similar to equations (2.4) – (2.6) except that the instantaneous velocity and pressure quantities are replaced by their mean components. It is noted that there are six extra terms, $\rho\overline{u'_j u'_i}$, found in the momentum equations. Known as the Reynolds stresses, these terms require six additional equations in order to fully solve the RANS equations. Directly solving these highly nonlinear coupled equations presents a significant computational hurdle. This is what is known as the closure problem in turbulence flow solving, and numerous models have been postulated which attempt to ease this computation expense.

2.2.1.4.1 Modelling Reynolds stresses

The basis of turbulence modelling lies in approximating the Reynolds stresses, which is usually accomplished through the use of a turbulent (eddy) viscosity term. The determination of this turbulent viscosity varies amongst different turbulence models. A particular class of turbulence models, known as *zero-equation* models, attempt to solve the turbulence directly from the known flow variables, using no additional transport equations. Due to this simplistic treatment of turbulence, the use of these models is limited to all but the most basic flow scenarios. Another class of turbulence models, the *one-equation* models, attempts to solve the turbulence using one turbulence transport equation. Although this is an improvement on the zero-equation approach, these models are generally calibrated to specific flow conditions, limiting their applicability to a wide range of flows (an example of which is discussed in section 2.2.1.4.3). A third class of turbulence models, known as the *two-equation* models, is popular due to their ability to solve a range of practical flows. These models compute the turbulence using two turbulence transport equations, offering a good compromise of solution accuracy, robustness, and relatively small computational resources required for their use.

Most turbulence models are based on the *eddy viscosity approximation* developed by Boussinesq. It was assumed that turbulence mixing acts to diffuse momentum, and so the Reynolds stresses are treated as an increase in the effective viscosity,

$$-\rho\overline{u_j'u_i'} = \mu_t\left(\frac{\partial U_j}{\partial x_i} + \frac{\partial U_i}{\partial x_j}\right) \tag{2.14}$$

where μ_t is the turbulent viscosity. In the popular *k-ε* and *k-ω* turbulence models, a turbulence velocity scale is calculated based on the turbulent kinetic energy, *k*, and a turbulence length scale is calculated from two quantities in the turbulence field – the turbulent kinetic energy and either the rate of turbulence dissipation, *ε*, or the turbulence frequency, *ω*. The two-equation *k-ε* and *k-ω* models compute these velocity and length scales with separate transport equations. The turbulent viscosity is then calculated as a combination of the turbulence velocity scale and the turbulence length scale.

2.2.1.4.2 Modelling turbulent flow separation

Much attention has been given to the nature of flow separation around streamlined foils and bluff bodies in the literature (eg. Simpson, 1996). In turbulent flow around an airfoil, from which an analogy to the flow around an oar blade can be drawn, separation occurs due to an adverse pressure gradient on the suction side of the foil. As the flow deflects past the leading edge of the foil, a region of rotational flow is created in a boundary layer between the foil surface and the free stream flow. As the flow progresses downstream along the foil, this region of rotational flow thickens, eventually leading to a loss of lift on the foil. This rotational flow within the boundary layer is characterized by low Reynolds stresses, is dominated by the dissipation and diffusion of turbulence, and the mean flow velocity is highly influenced by the motion of large-scale eddies. These large-scale structures serve to transfer momentum and turbulent energy produced in the outer flow region towards the wall through turbulence diffusion (Simpson, 1996). Modelling the behaviour of these turbulent structures relative to the mean flow requires an accurate treatment of Reynolds stress transport in the turbulence equations.

2.2.1.4.3 Selecting a turbulence model

The Spalart-Allmaras (*S-A*) model is a one-equation turbulence model designed in particular for aerodynamic flows. Although its treatment of turbulence is inherently simpler than in the two-equation models, the S-A model is able to accurately resolve the transport of turbulent viscosity, which is crucial in predicting separating flows. In addition, the computational expense of a one-equation model as compared to a two-equation model is less, but not by any large amount. Although the S-A model shows favour for use in separating flow conditions, more versatile two-equation models were investigated.

The two-equation k-ε model (Jones & Launder, 1972) handles turbulence in free-shear flows quite well, but its treatment of the flow in the near-wall turbulent boundary layer is lacking. This is due to its handling of the turbulent viscosity, which it models as being related to the turbulent kinetic energy and turbulence dissipation as,

$$\mu_t \propto \frac{k^2}{\varepsilon} \tag{2.15}$$

This relation has been shown to fail in capturing the proper turbulent viscosity in the turbulent boundary layer, leading to a delayed prediction of separation (Menter, Kuntz, & Langtry, 2003). Although wall functions have been developed to model the flow within the boundary layer, they generally still fail to correctly predict flow separation.

In contrast, the two-equation *k*-ω model (Wilcox, 1988) resolves turbulence characteristics in the near-wall region much better than the *k*-ε model by relating the turbulent viscosity to the turbulent kinetic energy and turbulence frequency as,

$$\mu_t \propto \frac{k}{\omega} \tag{2.16}$$

The downside to the *k*-ω model is that it is very sensitive to values of ω in the free-shear flow region, and so it fails to accurately capture flow separation due a strong external adverse pressure gradient (Menter, 1992).

The shear stress transport (*SST*) model (Menter, 1994) overcomes the deficiencies of these two models in predicting turbulent flow separation by combining the strengths of each, transitioning from the *k*-ε model in free-shear flow regions to the *k*-ω model in near-wall regions using a blending function. The transport of turbulent shear stresses, which are important in the prediction of adverse pressure gradients as discussed earlier, are also included the eddy viscosity formulation. The SST model has been shown to accurately model flow separation from a foil in an adverse pressure gradient (Bardina, Huang, & Coakley, 1997), and accordingly was chosen as being the most appropriate for the present simulations.

2.2.1.4.4 The SST turbulence model

The transport equations for k and ω in the SST model (Menter, 1994) are defined as follows,

$$\frac{\partial}{\partial t}\rho k + \frac{\partial}{\partial t}\rho U_i k = P_k - \beta^* \rho \omega k + \frac{\partial}{\partial x_i}\left[\left(\mu + \sigma_{k3}\mu_t \frac{\partial k}{\partial x_i}\right)\right] \tag{2.17}$$

$$\frac{\partial}{\partial t}\rho \omega + \frac{\partial}{\partial t}\rho U_i \omega = \alpha \frac{\omega}{k} P_k - \beta \rho \omega^2 + \frac{\partial}{\partial x_i}\left[\left(\mu + \sigma_{\omega 3}\mu_t \frac{\partial \omega}{\partial x_i}\right)\right] + 2(1-F_1)\rho \sigma_{\omega 2}\frac{1}{\omega}\frac{\partial k}{\partial x_i}\frac{\partial \omega}{\partial x_i} \tag{2.18}$$

where F_1 is a blending function, smoothly switching between 0 and 1 as the distance to wall decreases, transitioning from the k-ε to the k-ω model,

$$F_1 = \tanh\left\{\left\{\min\left[\max\left(\frac{\sqrt{k}}{\beta^* \omega y}, \frac{500\nu}{y^2 \omega}\right), \frac{4\rho\sigma_{\omega 2}k}{CD_{k\omega}y^2}\right]\right\}^4\right\} \tag{2.19}$$

where y is the distance to the wall, ν is the kinematic viscosity, and $CD_{k\omega}$ is a limiter for the cross-diffusion term (equivalent to the last term in the ω–transport equation,

$$CD_{k\omega} = \max\left(2\rho\sigma_{\omega 2}\frac{1}{\omega}\frac{\partial k}{\partial x_i}\frac{\partial \omega}{\partial x_i}, 10^{-10}\right) \tag{2.20}$$

P_k is a limiter for the production of turbulence,

$$P_k = \mu_t S^2 \tag{2.21}$$

which includes the absolute value of the strain rate, S,

$$S = \sqrt{2S_{ij}S_{ij}} \tag{2.22}$$

The eddy viscosity modification in the SST model, which attempts to account for the transport of principal shear stresses, is defined,

$$\mu_t = \frac{\rho a_1 k}{\max(a_1\omega, SF_2)} \tag{2.23}$$

and F_2 is a similar blending function to F_1, smoothly switching from 0 to 1 as it approaches the wall,

$$F_2 = \tanh\left\{\left[\max\left(\frac{2\sqrt{k}}{\beta^*\omega y}, \frac{500\nu}{y^2\omega}\right)\right]^2\right\} \tag{2.24}$$

The coefficients (in general, λ_i) in the above equations are calculated by blending the corresponding coefficients from the k-ω model (denoted with subscript $_1$) and the k-ε model (denoted with subscript $_2$) using the relation,

$$\lambda_3 = F_1\lambda_1 + (1-F_1)\lambda_2 \tag{2.25}$$

The coefficients for SST model are given in Table 2.1.

Table 2.1: Coefficients for the SST turbulence model

a	0.31
β^*	0.09
α_1	5/9
β_1	3/40
σ_{k1}	0.5
$\sigma_{\omega 1}$	0.5
α_2	0.44
β_2	0.0828
σ_{k2}	1
$\sigma_{\omega 2}$	0.856

These governing equations for the flow are highly coupled and nonlinear, and accordingly, require the use of a commercial solver. The description of the commercial software used and the method of flow solving are described in section 2.2.5.

2.2.2 Domain model

The computational domain of the water flume in the present simulation matches the experimental conditions of Caplan and Gardner (2007b), and can be seen in Figure 2.1. Table 2.2 outlines relevant dimensions of the blade and water flume. The length of the flume was designed to ensure upstream and downstream conditions from the blade are uniform at the inlet and outlet boundaries.

Table 2.2: Dimensions of the blade and flume for the quarter-scale steady-state simulations

Blade	
Width	12.6 cm
Depth	6.25 cm
Projected area, A_{proj}	78.5 cm^2
Thickness	1.80 mm
Flume	
Width	64.0 cm
Length	128.0 cm
Depth	15.0 cm (+ 20.0 cm of air above)
Velocity, v_{flume}	0.75 m/s

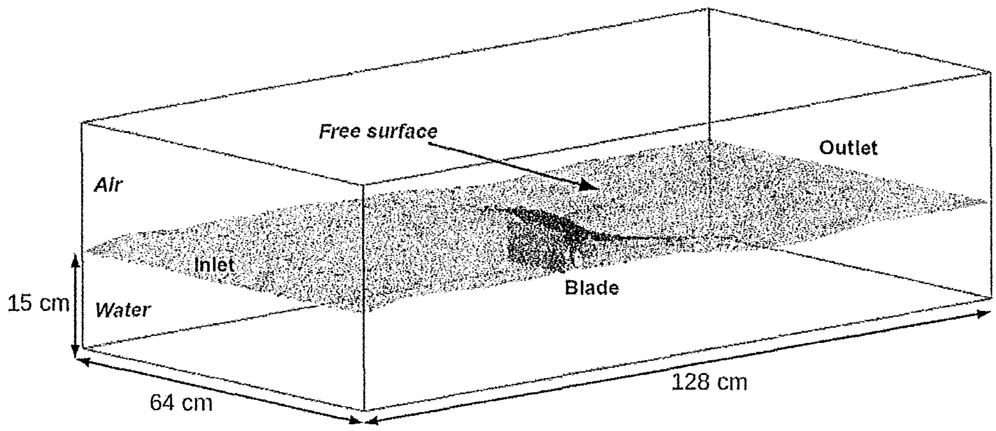

Figure 2.1: Domain for the steady-state quarter-scale blade simulations. Fluid flows in the left, around the blade, and exits at the right. The side and bottom surfaces are no-slip walls, and the top surface is a zero pressure gradient opening. The steady-state free surface is indicated

2.2.3 Boundary and initial conditions

At the inlet, a flume velocity, v_{flume}, of 0.75 m/s was specified, as in the experiments. As well, the bulk flow within the domain was initialized to this velocity prior to running the simulation. At the outlet, a zero relative static pressure boundary condition was imposed. The side walls and bottom surface of the flume were modelled as no-slip surfaces. The top surface was modelled as a zero relative static pressure opening to simulate the top of the flume being open to the environment as in the experiments.

Using the SST model, the turbulence intensity at the inlet, defined as the ratio of the turbulent velocity fluctuations to the mean fluid velocity ($I = u'/U$), is specified as 5%, and the turbulence length scale is equal the depth of the water (15 cm).

2.2.4 Mesh

An unstructured tetrahedral mesh for the domain was generated using ANSYS CFX-Mesh. A maximum element edge length of 4 cm was used away from the blade in the bulk flow region. To capture the detail of the flow around the blade, a maximum element edge length of 0.5 cm was applied on the blade surfaces. In addition, a 1.8 mm thick set of inflated boundary layer cells was included adjacent the blade and at the flume walls to provide small enough y^+ values required by the SST model to resolve the near-wall flow. To keep a sharp interface at the air and water boundary, three successive mesh refinements were performed during the solution stage. For each refinement, the size of the elements near the free surface was halved, thereby increasing the mesh resolution along the free surface. A grid refinement test was performed, and a 740,000 element domain mesh yielded grid-independent results, having less than a 1% difference in the resultant steady-state blade forces when compared to a 370,000 element mesh.

2.2.5 Flow solver

The conservation equations were solved using a scheme where a blending function switches between first- and second-order accurate advection schemes. In flow regions with low variable gradients, the blending function switches to a second-order scheme for accuracy, while in regions higher variable gradients, the blending function switches to the more robust first-order scheme. Turbulence quantities were solved using a first-order accurate advection scheme. A second-order accurate time advancement scheme was used for the conservation equations, and a first-order accurate transient scheme for the turbulence quantities. Using the ANSYS CFX-Solver CFD code, the governing equations were solved at each timestep until the root mean square (*RMS*) residuals of the mass and momentum conservation equations fell below 10^{-4}. The total simulation time was 5 s, and the monitored blade forces reached steady-state conditions by the end of the simulation. Although steady-state blade forces are obtained, a transient simulation was employed in order to resolve the initial flow conditions at startup. Timestep independence testing indicated that a 0.005 s time interval resolved the time dependencies of the flow. Simulations were repeated for α ranging from 0° to 180° at 15°

increments, and the results were used to calculate the drag and lift coefficients, which are examined in the proceeding section.

2.3 Validation of the numerical model

The streamwise (drag) force on the blade at each angle was converted to a drag coefficient, C_D, according to the relation,

$$C_D = \frac{2F_{drag}}{\rho A_{proj} v_{flume}^2} \tag{2.26}$$

Lift coefficients were calculated similarly using the spanwise (lift) force.

Comparing the drag and lift coefficients calculated from the simulation to those from the experiments (Caplan & Gardner, 2007b), a very good agreement over the range of attack angles is seen (Figure 2.2). The simulated coefficients are slightly lower (~ 10%) than the experimental values, however, and this difference is most pronounced near the peaks of each curve. It is noted that in Caplan and Gardner's experiments, due to the way in which the support shaft was connected to the blade, part of the shaft was below the water surface. It is possible that this increased surface area of the blade apparatus exposed to the flow would lead to an overestimation of the experimental flow coefficients, which would explain the discrepancy in the results between the experiments and the simulation. The ability of the present simulation to replicate the quarter-scale blade experimental results validates the numerical model, providing confidence in its ability to handle similar flows.

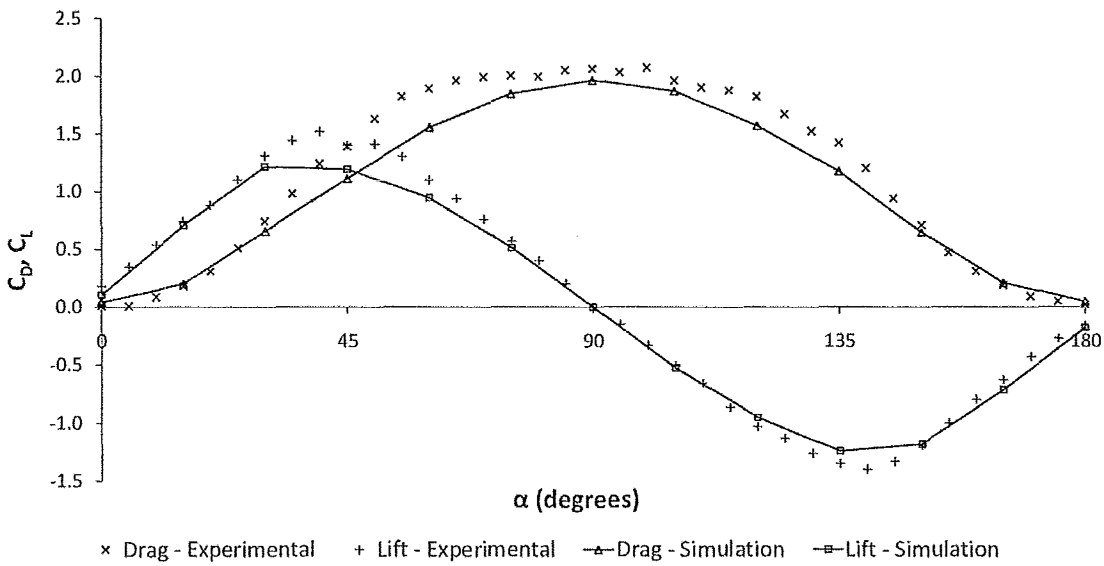

Figure 2.2: Comparison of experimental and simulated drag ($C_D = 2F_{Drag}/\rho A_{proj}\ v_{flume}^2$) and lift coefficients ($C_L = 2F_{Lift}/\rho A_{proj}\ v_{flume}^2$) for a quarter-scale steady-state blade in a water flume for values of angle of attack, α. The numerical model uses the same flume dimensions, projected blade surface area, A_{proj} (78.5 cm^2), and flume velocity, v_{flume} (0.75 m/s) as the experimental results (Caplan & Gardner, 2007b). Experimental coefficients are plotted in 5° increments as points, and the simulatted coefficients are plotted in 15° increments as points connected by straight lines

2.4 Full-scale blade in open water simulations

The steady-state drag and lift coefficients for a quarter-scale oar blade in a flume cannot be assumed to be the same as those for a full-scale blade in open water conditions because there is evidence that these flows are not similar. Although a flume velocity greater than 0.7 m/s was stated to be Reynolds number (Re) independent (Caplan & Gardner, 2007b), Coppel *et al.* (2008) found that the 0.75 m/s flume velocity was in fact not within the range of Reynolds number independence. Coppel *et al.* performed numerical simulations of the quarter-scale blade flume experiments and of a full-scale blade in a geometrically similar (i.e. both the blade and the flume were four times larger) domain with a flow velocity of 5 m/s. The water surface was unrealistically modelled as a flat symmetry plane. In spite of this shortcoming of the model, a comparison of the calculated drag and lift coefficients between these simulations revealed that lift characteristics at both scales were similar, but the drag at quarter-scale was substantially larger than at full-scale. In addition, these simulations did not address whether the relatively tight proximity of the blade to the flume walls affects drag and lift characteristics as compared to open water conditions.

The next step in modelling the flow around an oar blade involves a steady flow analysis for a full-scale blade in realistic open water conditions. Drag and lift coefficients from this simulation will be compared to those for the quarter-scale blade in a flume, providing insight into the differences between these flows.

2.4.1 Domain model

Similar to the quarter-scale blade simulation, the length of the full-scale domain was set to ensure uniform bulk flow conditions at the inlet and outlet. The blade was located in the centre of the domain, and the width and depth of the domain was specified such that the influence of the walls would have minimal impact on the flow around the blade. The domain width is approximately 20 times greater than blade width at 90° (compared to only 5 times greater in the quarter-scale flume) and the domain depth is 6 times greater than the blade depth (compared to only 2.4 times greater in the quarter-scale flume). These dimensions were tested to ensure that the flow streamlines were essentially linear at half of the the distance from the blade edges to the walls. The curved plate representing the blade was four times larger than the quarter-scale blade, having the same projected surface area as a standard hatchet blade. Dimensions of the full-scale model are outlined in Table 2.3.

Table 2.3: Dimensions of the blade and flume for the full-scale steady-state simulations

Blade	
Width	50.4 cm
Depth	25.0 cm
Projected area, A_{proj}	1260 cm^2
Thickness	5.0 mm
Flume	
Width	10.0 m
Length	10.0 m
Depth	1.5 m (+ 0.5 m of air above)
Velocity, v_{flume}	2.5 m/s

2.4.2 Boundary and initial conditions

The boundary and initial conditions for the full-scale blade simulation were the same as for the quarter-scale simulation, except for the flume walls, which were now modelled as free-slip. The flume inlet velocity was set at 2.5 m/s, which is less than the velocity used in the full-scale blade simulations (5 m/s) by Coppel *et al.* (2008), but is more indicative of the relative velocity incident on the blade throughout the stroke (Kleshnev, 2007). The bulk flow through the domain was also initialized to 2.5 m/s prior to the start of the simulation.

2.4.3 Mesh and flow solver

An unstructured tetrahedral mesh similar to that for the quarter-scale blade flume simulation was generated. The maximum element edge length in the flow away from the blade was 10 cm, while adjacent to the blade surfaces it was 0.5 cm. A 3 mm thick set of inflated boundary layer cells was included on the blade surface, providing appropriate y^+ values required for the SST turbulence model. Grid refinement testing indicated that this mesh, with 2.8 million elements, produced grid-independent results when compared to a 1.4 million element mesh.

The simulations were solved using both the 2.8 million element mesh (without further refinement), and using the mesh refinement procedure that was used in the quarter-scale blade flume simulations. The shape of the free surface resolved in both simulations was very similar, and the resultant blade forces from both were also within 1% of each other. This reveals that the initial grid for this simulation is capable of resolving the free surface flow behaviour as well as the refined grid.

The unsteady turbulent multiphase Navier-Stokes equations (Equations (2.11) – (2.13)) were solved using the SST turbulence model as before for α ranging from 0° to

180° in 15° increments. A 0.005 s timestep was used and the simulations were run for 5 s, allowing the monitored blade forces to reach steady-state conditions.

2.4.4 Comparison of quarter-scale flume and full-scale open water flows

A comparison of the simulated drag and lift coefficients from this full-scale flow with those from the modelled quarter-scale flow reveal substantial differences in magnitude (Figure 2.3). Although the shape of the coefficient curves is similar, the full-scale blade drag and lift values are between 20% - 30% lower than the quarter-scale values over the full range of α.

The lower drag and lift coefficients in the full-scale open water simulation are attributed to several factors. The increased spacing between the blade and the walls in the present domain model are more representative of open water conditions, allowing the flow to deflect around the blade at greater distances which in turn affects drag and lift. The proximity of the blade to the flume walls also affects the free surface behaviour around the blade and in its wake, further impacting blade drag and lift characteristics. In addition, the fluid velocity of 0.75 m/s for the quarter-scale blade flume corresponds to a Reynolds number of approximately 10^5, while the 2.5 m/s velocity for the full-scale blade in open water leads to a Reynolds number of approximately 10^6. The large difference in magnitude of the Reynolds number for the two blade flows influences the values of the drag and lift coefficients, similar to what was earlier shown by Coppel *et al.* (2008).

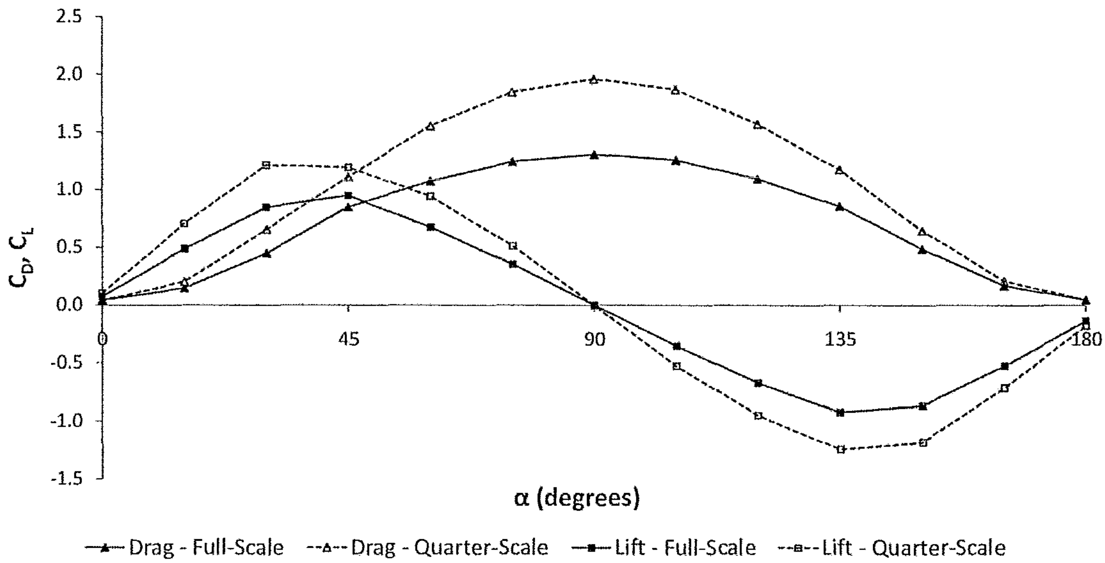

Figure 2.3: Comparison of steady-state drag ($C_D = 2F_{Drag}/\rho A_{proj}\ v_{flume}{}^2$) and lift coefficients ($C_L = 2F_{Lift}/\rho A_{proj}\ v_{flume}{}^2$) for a quarter-scale blade in a water flume with a full-scale blade in open water for values of angle of attack, α. The projected surface area, A_{proj}, of the quarter-scale blade is 78.5 cm^2, and the water velocity, v_{flume}, is 0.75 m/s. The projected surface area, A_{proj}, of the full-scale blade is 1260 cm^2, and the water velocity, v_{flume}, is 2.5 m/s. Quarter-scale blade coefficients are plotted as open symbols connected by dashed straight lines, and full-scale blade coefficients are plotted as filled symbols connected by straight lines

The effect of Reynolds number on steady-state blade flow will not be investigated further. As it has been discussed, the velocity of the relative flow incident on the blade changes substantially through the duration of a stroke, and also varies across the surface at a given instant of time. This characteristic of unsteady blade flow, combined with temporally developing flow conditions (such as free surface deformations and vortices) likely limits the relevance of a steady-state flow analysis. As a result, the steady-state flow coefficients for a blade in open water conditions, with a bulk flow velocity of

2.5 m/s, will simply be used as a basis from which to compare the coefficients for an unsteady blade in section 3.3.

3 Unsteady Analysis

3.1 Rowing stroke simulation

The steady-state experiments and simulations of the previous chapter determined the drag and lift behaviour of an oar blade over a range of static angles of attack. However, it is not clear how these characteristics are affected by the rapidly changing angle of attack throughout a stroke. To model the unsteady hydrodynamic conditions of a rowing blade in motion, the steady-state computational model was modified to allow for blade rotation, and an analytical force-based shell velocity model was created to account for the varying shell velocity during a stroke.

3.1.1 Domain model, boundary and initial conditions, and mesh

Like the full-scale steady domain model, the unsteady simulation was designed with a full-scale rectangular blade. With a frame of reference based on an accelerating shell, the model accommodates blade rotation by including an 8 m diameter cylindrical rotating domain (containing the blade) nested within an outer stationary domain (Figure 3.1). The outer stationary domain retains the same dimensions as the full-scale steady-state domain, which is sufficiently large as to represent open water conditions. The tip edge of the blade is located in the rotating domain at a radial distance of 2.4 m from the axis of rotation (representing the oarlock). This radial position of the blade corresponds to the outboard length of the oar. As with the steady-state simulations, the top edge of the blade is flush with the surface of the water at the beginning of the drive.

The interface between the outer stationary domain and the inner rotating domain allows fluid to cross seamlessly, and a rigid mesh within the rotating domain allows oar rotation by rotating the entire cylindrical domain itself. Specifying the instantaneous angular velocity of the rotating domain then simulates oar rotation. The varying shell velocity through the stroke is simulated by the bulk flow through the domain, flowing in the same manner as in the full-scale steady simulation and with similar boundary conditions. Although the blade becomes nearer to the side walls during the middle portion of the stroke, the width of the domain was tested to ensure that the walls have a negligible impact on the flow around the blade.

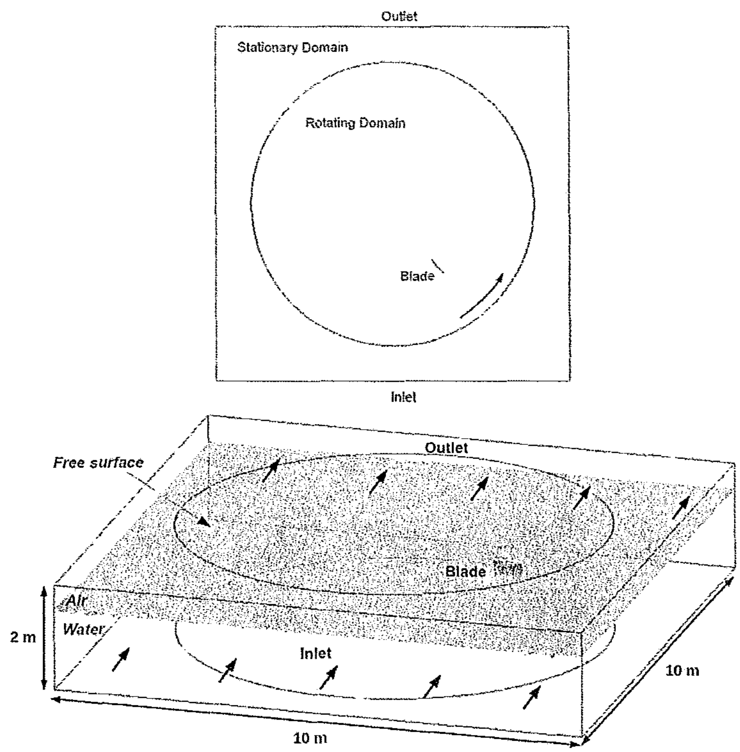

Figure 3.1: Overhead and isometric views of the unsteady domain model. The inner cylindrical rotating domain, containing the blade, is nested in the centre of the stationary domain and rotates counter-clockwise. The inlet and outlet boundaries are indicated, in addition to the location of the free surface. The sides and bottom surfaces are free-slip walls and the top surface is a zero relative static pressure gradient opening

An unstructured tetrahedral mesh with the same element edge length and boundary layer cell specifications as the full-scale steady-state blade simulations was created. Similar to the full-scale open water domain, grid testing indicated that this mesh, with 2.8 million elements, produced grid-independent results when compared to a 1.4 million element mesh. No mesh refinement was used during the solution stage, as the original grid was found to be grid-independent (as described in section 2.4.3).

3.1.2 Numerics

To account for the unsteady bulk flow through the domains and for the flow within the rotating circular domain, several source terms, denoted S_M, need to be added to the streamwise and spanwise components (x- and y-components, respectively) of the momentum equation (Equation (2.13)),

$$\frac{\partial}{\partial t}(\rho U_j)+\frac{\partial}{\partial x_i}(\rho U_i U_j)=-\frac{\partial P}{\partial x_j}+\frac{\partial}{\partial x_i}\left[(\mu+\mu_t)\left(\frac{\partial U_j}{\partial x_i}+\frac{\partial U_i}{\partial x_j}\right)\right]-\rho g_j+S_M \tag{3.1}$$

In the streamwise (x-component of the) momentum equation, a source term, S_{shell}, is included to allow a uniform shell acceleration throughout the domain,

$$S_{shell}=\rho a_{shell} \tag{3.2}$$

There are three additional source terms included in the streamwise and spanwise (x- and y-components, respectively, of the) momentum equation for the flow within the rotating domain. These terms account for the effect of the Coriolis force, centrifugal force, and an Euler force associated with the non-uniform angular acceleration of the domain,

$$S_{Coriolis}=-2\rho\omega_{oar}\times v_{shell} \tag{3.3}$$

$$S_{centrifugal}=-\rho\omega_{oar}\times(\omega_{oar}\times r) \tag{3.4}$$

$$S_{Euler}=-\rho\frac{\partial\omega_{oar}}{\partial t}\times r \tag{3.5}$$

where r is the radial location from the centre of the domain.

The SST turbulence model was once again chosen. In addition to the ability of the SST model to predict flow separation from a stationary airfoil as described earlier, it has also demonstrated success in predicting separation on unsteady airfoils (Ekaterinas & Menter, 1994). Their flow simulations featured a pitching airfoil having a reduced frequency of 0.1 in a 2×10^6 Reynolds number flow, with angles of attack ranging from $0° – 20°$. They found that of the numerous one- and two-equation turbulence models tested, the SST model was the best predictor of the separation behaviour and of the shape of the hysteresis loops.

3.1.3 Analytical rowing shell velocity model

The rowing shell velocity model is based on force balances on the shell and the rowers. By specifying an oar angular velocity and the motion of the crew with respect to the shell, the shell velocity is calculated based on the propulsive force generated by the blade in the water, an analytical treatment of the drag on the shell, and the momentum of the crew. The force balance is stated,

$$F_{net,shell} = F_{propulsive,crew} + F_{momentum,crew} + F_{drag,shell} \tag{3.6}$$

where,

$$F_{propulsive,crew} = n_{oars} \cdot F_{propulsive} \tag{3.7}$$

$$F_{momentum,crew} = m_{crew} \cdot a_{relative,crew} \tag{3.8}$$

$$F_{drag,shell} = k_{drag} \cdot v_{shell}^2 \tag{3.9}$$

In Equation (3.7), the combined propulsive force generated by the crew, $F_{propulsive,crew}$, is the propulsive force provided by a single oar, $F_{propulsive}$, multiplied by n_{oars}, the number of oars.

The momentum of the back-and-forth motion of the crew within the shell, $F_{momentum,crew}$, substantially affects shell velocity. In the present model, it is assumed that each rower is a point mass located at their centre of mass and are all perfectly synchronized with one another. The effect of rower momentum is determined using Equation (3.8), which is based on the mass of the crew, m_{crew}, and their instantaneous acceleration relative to the shell $a_{relative,crew}$. This acceleration is calculated using the velocity of the crew with respect to the shell, $v_{relative,crew}$ (Figure 3.2), which was derived by Atkinson (personal communication, April 2009) based on approximations of the position of the components of a rowers body throughout the stroke in relation to a known oar angular rotation.

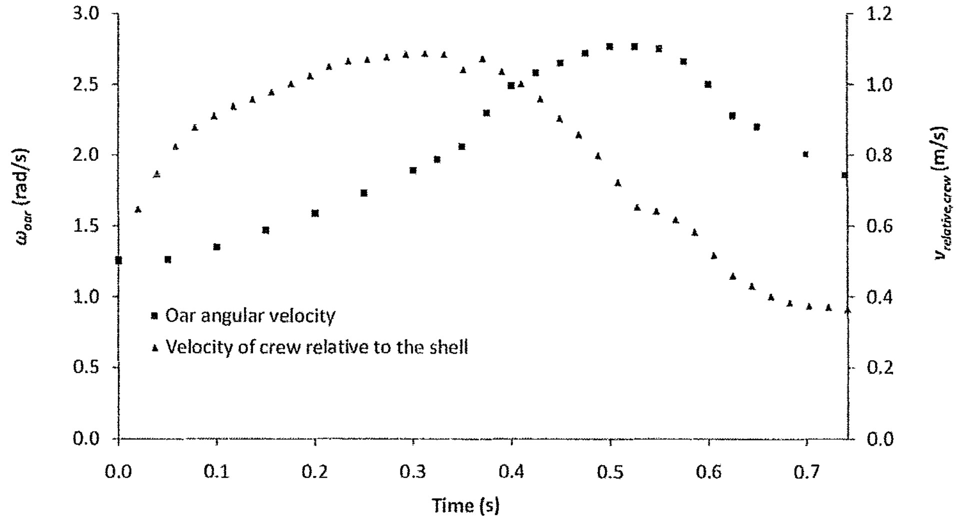

Figure 3.2: Oar angular velocity during the drive, indicated by square data points, and velocity of the crew relative to the shell, indicated by triangular data points (based on Kleshnev and Atkinson, personal communication, 2009)

The hydrodynamic drag force experienced by the shell, $F_{drag,shell}$, can be subdivided into skin friction drag, caused by viscous forces where water is in contact with the shell; form drag caused by the momentum transferred from the shell to the water; and wave drag from the energy required to sustain a moving wave pattern. Experiments carried out by Wellicome (1967) indicated that skin friction accounts for roughly 93% of the hydrodynamic drag, and is highly dependant on the shell velocity. In Equation (3.9), the drag force acting on the shell is a function of the square of the instantaneous shell velocity, v_{shell}, and a constant drag factor, k_{drag}, where,

$$k_{drag} = (1.07)\,{}^{1}\!/_{2}\, c\rho A_{shell} = 6.0\frac{N}{(m/s)^2} \tag{3.10}$$

and A_{shell} is the wetted surface area of the shell (area of the hull that is in contact with the water). The nondimensional skin friction drag coefficient ($c = 0.00225$) was calculated using the ITTC 1957 Hull Friction Resistance Correlation Line (International Towing Tank Conference, 2002),

$$c = \frac{0.075}{(\log_{10} \mathrm{Re}_D - 2)^2} \tag{3.11}$$

where Re_D is the Reynolds number for the submerged length of the shell. This value is close to an experimental coefficient of 0.00224 determined by Wellicome (1967) for an eight-oared shell. This similarity was expected, as a study by McMahon (1971) revealed the geometric similarity of rowing shells of different sizes. The factor of 1.07 is included to account for form and wave drag (Wellicome, 1967). Although wave drag is dependant on numerous variables (velocity, water depth, etc.), its approximation as a constant multiplier of the skin friction drag is assumed to be sufficient for the narrow range of low velocities characteristic of a rowing shell. Air drag on the shell, oars, and rowers, which are minimal in comparison to the hydrodynamic drag (Wellicome, 1967) is ignored.

Using the instantaneous net force on the shell from equation (3.6), $F_{net,shell}$, and the combined mass of the crew and shell, m_{total}, shell acceleration can be calculated as,

$$a_{shell} = \frac{F_{net,shell}}{m_{total}} \tag{3.12}$$

The flow velocity is updated at each timestep, Δt, based on the shell velocity at the previous timestep ($v_{shell,t-1}$) and a_{shell} using the relation,

$$v_{shell,t} = v_{shell,t-1} + a_{shell} \cdot \Delta t \tag{3.13}$$

To simulate the motion of the shell at the catch, the bulk flow within the domain is initialized to match the shell velocity immediately at the beginning of the drive. A smooth blade entry into the water at the catch is similarly modelled by initializing the angular velocity of the rotating domain to match the oar angular velocity at the beginning of the drive.

3.1.4 Assumptions in the rowing shell velocity model

Numerous conditions of the rowing stroke, the equipment, and the environment were assumed when creating the model. These assumptions do not detract from the ability of the model to replicate an actual rowing stroke, rather they simply represent ideal conditions. The motion of the shell and the rowers were assumed to act linearly along the axis of the shell. Any heaving or pitching motion of the shell that may occur from a vertically changing centre of mass or rolling motion from a lateral imbalance of the crew is ignored. In addition, torques created by the oars on either side of the shell are assumed to balance. The oars themselves are considered massless, as the oar mass in a shell being rowed by four heavyweight men is less than 1% of the total mass. The oars are also considered to be perfectly stiff, as justified from Cabrera, Ruina, & Kleshnev (2006). In the present model, as with actual oars, the blade chord line is parallel to the shaft. That is, when the oar shaft is at a given angle, the blade chord is at the same angle. In addition, there is no blade pitch, meaning the blade sits perfectly vertical in the water through the stroke. Real oar blades commonly rest in the water with a slight pitch (~ 4°) to aid the rower in keeping the blade at a constant water depth through the stroke. However, an ideal sweep of the blade with respect to the shell follows essentially a horizontal trajectory, as in the present model. The water conditions are still, and there is no current or wind. The water depth (1.5 m) also represents the approximate depth occurring on many rowing courses. Although wave drag for a shell has been shown to be a function of water depth (Wellicome, 1967), its minor contribution to the overall drag force, as mentioned earlier, suggests that small variations in depth would have a negligible effect on shell drag. Finally, it is assumed that the rowing stroke is occurring at *steady state*, where the crew is rowing at an established stroke rate and with a constant average velocity.

3.1.5 Modelled stroke quantities

To provide a basis for comparison of the results, the physical parameters of the rowing stroke were set to match those used in Kleshnev's experiments involving a shell with four sweep rowers (each holding one oar) being rowed in actual conditions (Table 3.1). In his experiments, Kleshnev instrumented rowing equipment to obtain data relating the linear velocity of the shell to the oar angular velocity during a stroke. Details of these measurement techniques are available (Kleshnev, 1999). The oar angular velocity, ω_{oar}

(Figure 3.2), specified as an input in the present simulation is based on experimental data from Kleshnev (personal communication, April 2009).

Table 3.1: Parameters of the rowing stroke (Kleshnev, personal communication, 2009)

Boat class	Heavy Men 4-
Crew weight (m_{crew})	376 kg
Shell weight (m_{shell})	50 kg
Shell wetted area (A_{shell})	5 m^2
Oar outboard length	2.4 m
Stroke rate	31.1 spm
Stroke period	1.93 s
Drive period	0.74 s

3.1.6 Flow solver

Timestep testing indicated that a 0.005 s interval resolved the time dependencies of the flow, with less than a 1% difference in the calculated shell velocity at each timestep when compared to a 0.01 s step size. Using the ANSYS CFX commercial CFD code, the governing equations were solved at each timestep until the RMS residuals of the mass and momentum conservation equations fell below 10^{-4}, and the blade forces stabilized.

3.2 Validation of the shell velocity model

The primary source of validation for the model lies in its ability to predict the shell velocity pattern during a stroke. Figure 3.3 plots the shell velocity during both the drive and recovery phases for the simulation along with experimental values obtained by Kleshnev (personal communication, 2009). The recovery phase of the stroke is modelled identically to the drive phase, except for the absence of the propulsive force term,

$$F_{net,shell} = F_{momentum,crew} + F_{drag,shell} \tag{3.14}$$

The shell velocity at the end of the stroke cycle (and thus immediately before the next cycle begins) is within 1% of the shell velocity at the beginning of the stroke. This occurs after the first iteration of a complete stroke simulation, which is expected for a crew that is rowing at, and maintaining, an established stroke rate and a constant average velocity. The simulated shell velocity through the stroke follows the same shape as observed in the experiment, although the average shell velocity from the simulation is 4.1% lower than the experimental value.

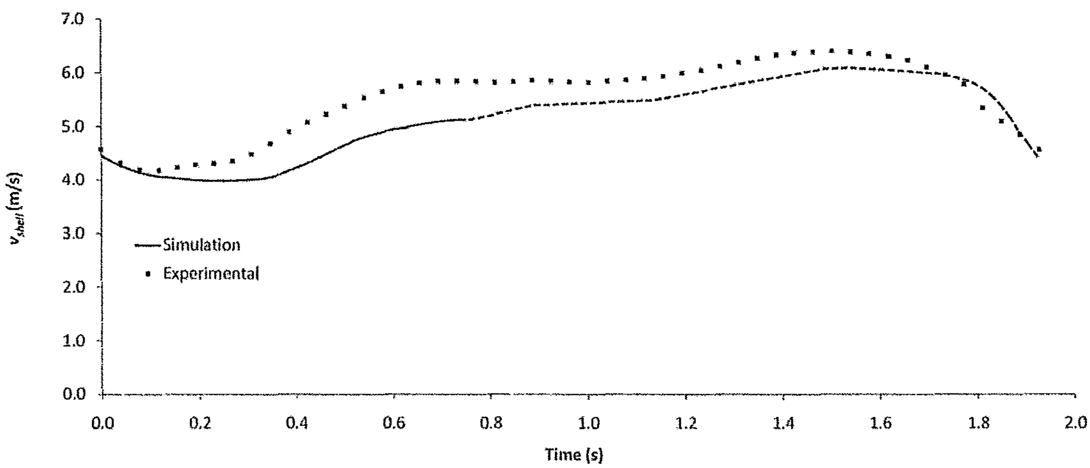

Figure 3.3: Comparison of simulated and experimental shell velocity during the stroke. The simulation data for the drive is indicated with a solid line, and for the recovery with a dashed line. The experimental data is from Kleshnev (personal communication, 2009)

Observing the motion of the centre of the blade chord through the water from a stationary reference frame, it follows a *figure-9* pattern (Figure 3.4) similar to what has been observed in experiments (Figure 1.3). In addition, a qualitative examination of the evolution of the free surface around the blade indicates an agreement with what is observed in real rowing conditions (Figure 3.5). After blade insertion at the catch, there is minimal disturbance of the free surface. As the stroke progresses, there is a growing surface bulge over the top edge of the blade, and surface depression behind the blade.

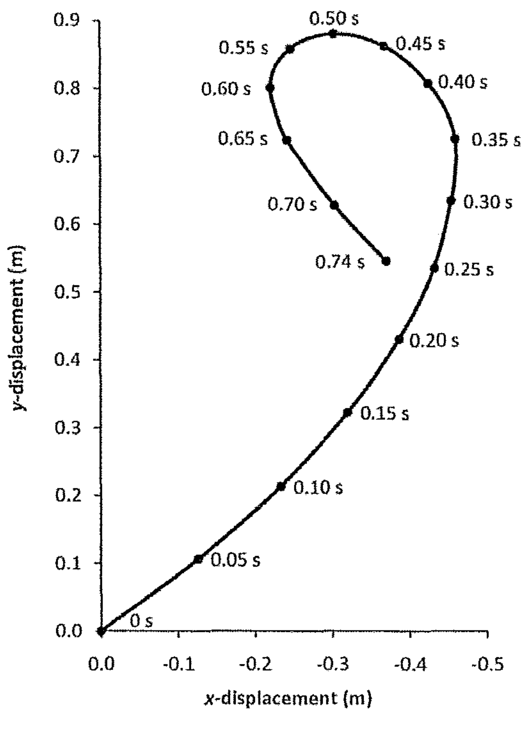

Figure 3.4: Taken from the present simulation, an overhead view from a stationary frame of reference indicating the calculated path of the centre of the blade chord line through the water during a stroke. The shell is moving from left to right

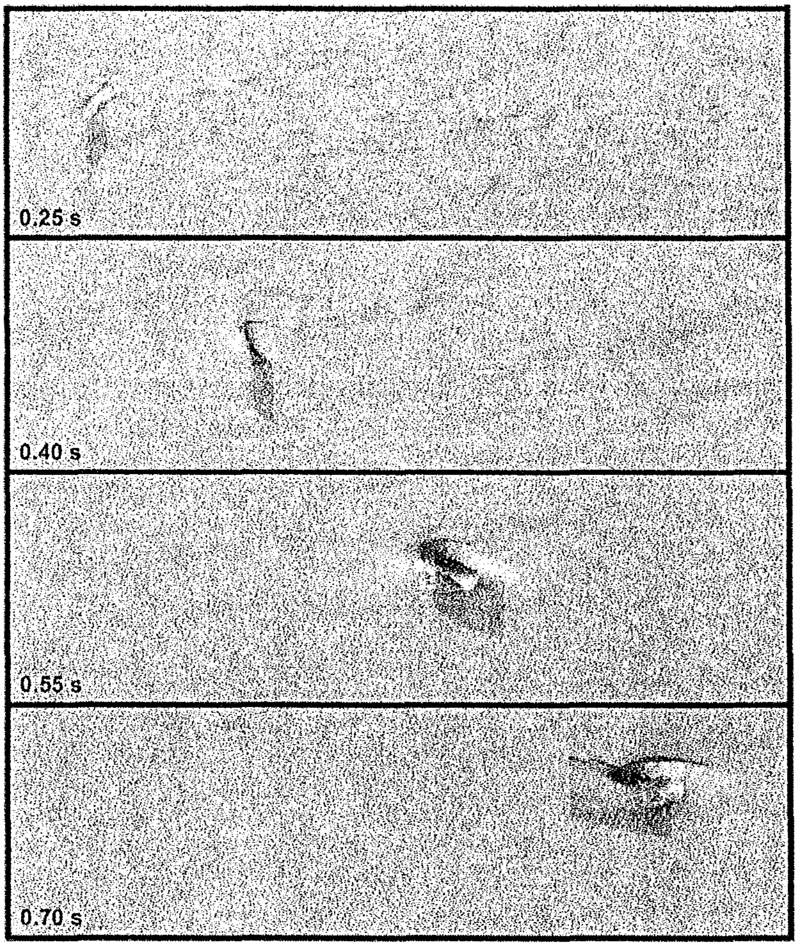

Figure 3.5: Evolution of the free surface throughout the stroke. The flow is moving along with the blade sweeping from left to right (meaning the shell is moving from right to left)

The simulation is highly sensitive to the input of an oar angular velocity which is based on experimental values, and a relative crew velocity which is modelled based in part on a given oar angular position. Any errors in these temporal input values likely have a significant impact on the resultant shell velocity. The steep drop in the simulated shell velocity as compared to the experimental value near the end of the recovery suggests that the modelled motion of the crew with respect to the shell maybe be susceptible to error. If this is the case, the discrepancy in the resultant shell velocity might be more to blame on the modelled crew motion than on the resolved blade hydrodynamics. In addition, as described earlier, the shape of the blade in the simulation is a curved rectangle with the same surface area as a hatchet blade. Although this geometry is not the same as was used in the experiments, it represents a good approximation to an actual rowing blade, for which dimensional data was unavailable. This geometry is also one that has been used in previous studies investigating drag and lift effects for stationary blades (Caplan & Gardner, 2007b). That the model is able to simulate the shape of the experimental shell velocity profile and produce qualitatively good representations of the shape of the blade path traced in the water and of the free surface, it gives confidence that it is able to replicate the physics of the rowing stroke and capture the hydrodynamic characteristics of a blade in motion.

3.3 Unsteady blade coefficients

From the calculated flow and pressure fields around the blade throughout the drive, the resultant force on the blade can be determined. This force can be broken down into drag and lift forces, and converted to drag and lift coefficients. These coefficients are compared to those determined for the steady-state open water blade simulations over the range of $\alpha_{nominal}$ (Figure 3.6).

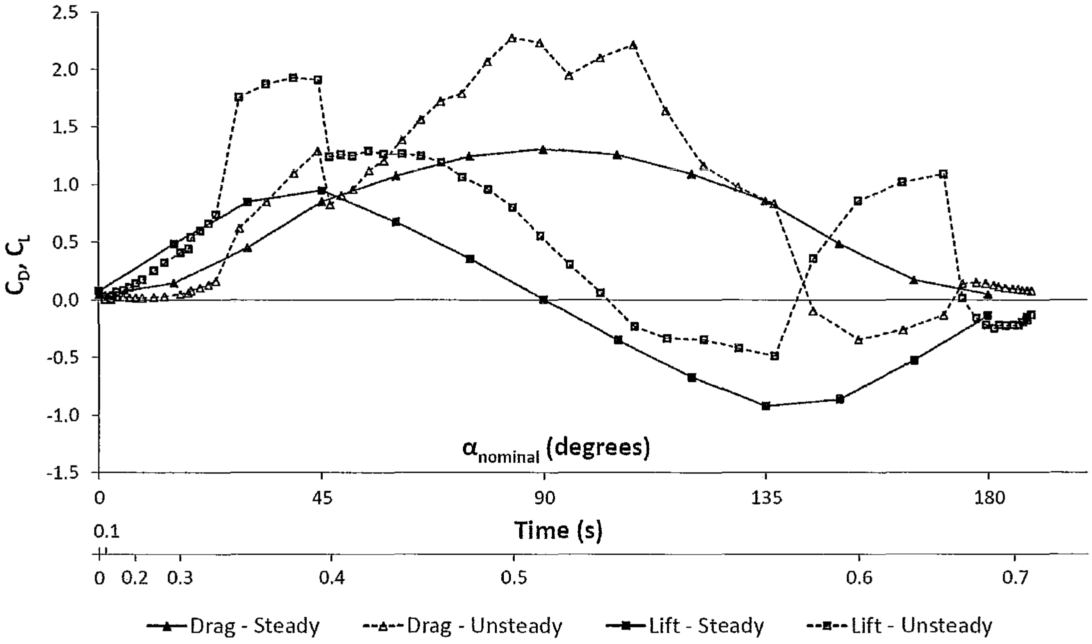

Figure 3.6: Comparison of steady and unsteady drag ($C_D = 2F_{Drag}/\rho A_{proj}v^2$) and lift coefficients ($C_L = 2F_{Lift}/\rho A_{proj}v^2$) for a full-scale blade in open water for values of nominal angles of attack, $\alpha_{nominal}$. The projected surface area of the blade, A_{proj}, is 1260 cm^2 and v is the relative flow velocity incident on the blade. Steady-state blade coefficients are plotted as solid points connected by solid straight lines, and unsteady blade coefficients are plotted as hollow points connected by dashed straight lines. The time axis applies to the unsteady data

The drag and lift coefficients produced from the unsteady simulation show a rough trend with the steady data. Through the first 0.35 s of the stroke period, $\alpha_{nominal}$ increases very slowly, staying below 25°. The unsteady lift and, particularly, drag coefficients at these low $\alpha_{nominal}$ values are beneath those predicted from the steady simulation, and are steadily increasing along with the nominal angle of attack, which is typical of pitching airfoils (McCroskey, 1982). From 0.35 s to approximately 0.6 s,

$\alpha_{nominal}$ increases rapidly from 25°, becoming square to the face of the blade (90°), then further increasing to 135° (analogous to 45° as seen from the shaft-side of the blade). In this range, the unsteady drag and lift coefficients roughly follow the trend of the steady values, although the unsteady values are higher in magnitude. There are, however, several large differences in these unsteady coefficients. After 0.35 s there is a spike in the drag and lift coefficients as $\alpha_{nominal}$ begins to rapidly increase. These values continue to increase, albeit at a slighter rate, until 0.4 s when they suddenly drop. Also, between approximately 0.59 s and 0.63 s there is an unusual behaviour of the drag and lift coefficients, as they are directed opposing (and with a relatively high magnitude) the shell velocity. The switched signs of the drag and lift coefficients are attributed to the direction of the resultant blade force vector, opposing the relative flow on the blade. For the last portion of the stroke, the flow is incident on the convex face of the blade ($\alpha_{nominal} > 180°$), for which there is no steady-state data. The low drag and lift coefficients in this region are expected based on the relatively low $\alpha_{nominal}$.

A comparison of drag and lift coefficients between the steady and unsteady cases was meant to merely highlight that the hydrodynamics of a blade in motion differ from a stationary blade. Investigation into the underlying causes of these differences in drag and lift behaviour, and its net result on the generated propulsive blade force will be investigated in the following section.

3.4 Flow phases during the rowing stroke

The component of the blade force in the direction of the shell motion (the propulsive force, $F_{propulsive}$) in addition to the blade drag and lift force components are plotted in Figure 3.7. Based on these forces, and on the relative blade motion in the water (Figure 3.4), it is observed that there are six distinct flow regimes encountered during the drive. These flow phases are outlined in Table 3.2. A detailed examination of the flow throughout the stroke gives insight as to the mechanisms defining each phase.

Table 3.2: Behaviour of blade forces, as well as the nature of slip, in each phase of the drive

Phase	Time (s)	$F_{propulsive}$	F_{drag}	F_{lift}	Slip
I	0 - 0.35	low	very low	low	positive
II	0.35 - 0.4	very high	moderate	very high	negative
III	0.4 - 0.5	high	high	moderate	negative
IV	0.5 - 0.6	moderate	moderate	low	negative
V	0.6 - 0.65	negative	negative	negative	positive
VI	0.65 - 0.74	very low	very low	low	positive

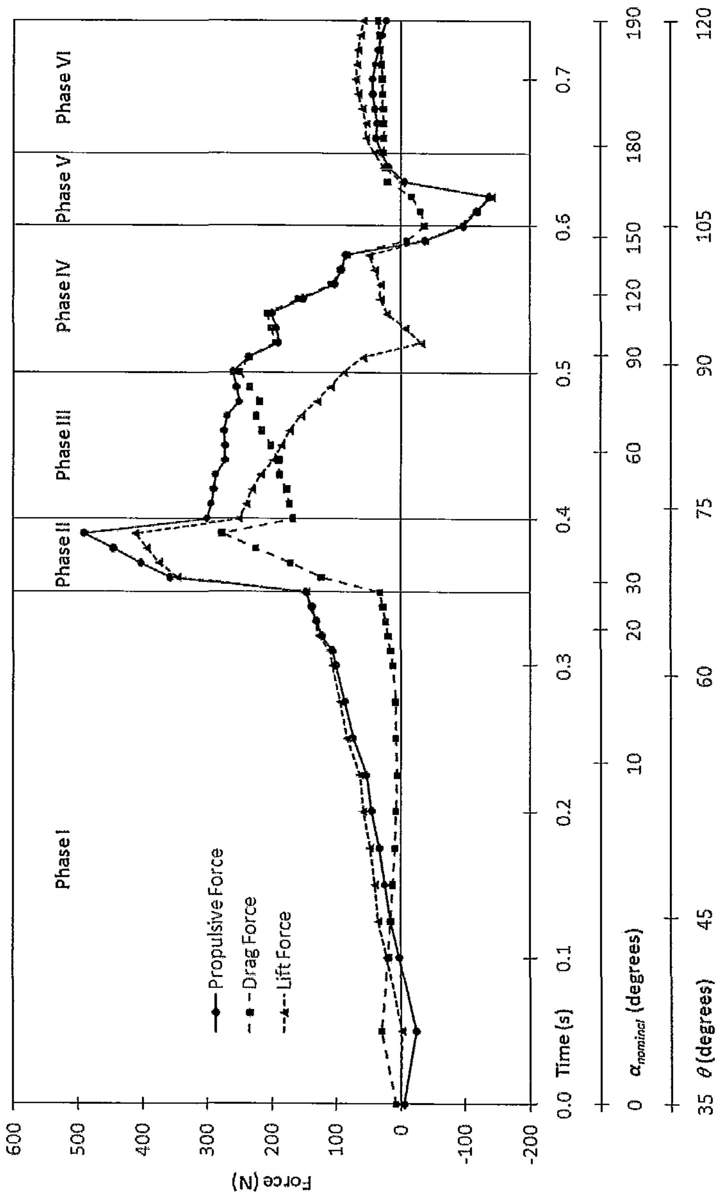

Figure 3.7: Temporal development of forces on the blade during a stroke, divided into six phases. The propulsive force is indicated by a solid line, drag force by a dashed line, and lift force by a dotted line. Additional abscissa axes include the nominal angle of attack on the blade and the bow-angle of the oar

3.4.1 Phase I

From blade entry in the water at the catch ($t = 0$ s) until 0.35 s, Phase I accounts for nearly half of the drive time. Immediately after entering the water at the beginning of the drive, the blade moves both laterally away from the shell, and with a positive slip (Figure 3.4). The blade experiences a shallow but gradually increasing $\alpha_{nominal}$ during this phase, rising from 0° to 25° (Figure 3.8 a). As $\alpha_{nominal}$ increases, there is an increasing pressure difference across the blade (up to ~ 1.5 kPa) located near the tip, which is mostly due to the increasing flow velocity over the back surface of the blade (Figure 3.8 b). Initially, the flow is almost entirely horizontal along the blade, moving from the tip edge toward the shaft. As $\alpha_{nominal}$ increases, flow begins to spill over the top and bottom edges of the blade, and small horizontal vortices with their cores aligned horizontally parallel to the top and bottom edges of the blade are formed on the back surface (Figure 3.8 c). These vortices aid in keeping the flow attached to the back of the blade throughout this phase, even when the angle of attack at the blade tip is approximately 25°, which in turn keeps drag minimal. The flow over the top edge of the blade also leads to a growing surface deformation (Figure 3.8 d). Toward the end of this phase, a small flow separation near the blade tip occurs, caused by the formation of a vertical vortex with its core aligned parallel to the tip edge (Figure 3.8 c). The resulting suction effect on the back of the blade leads to an increasing lift force. Correspondingly, the propulsive force in Phase I is primarily due to lift on the blade (Figure 3.7).

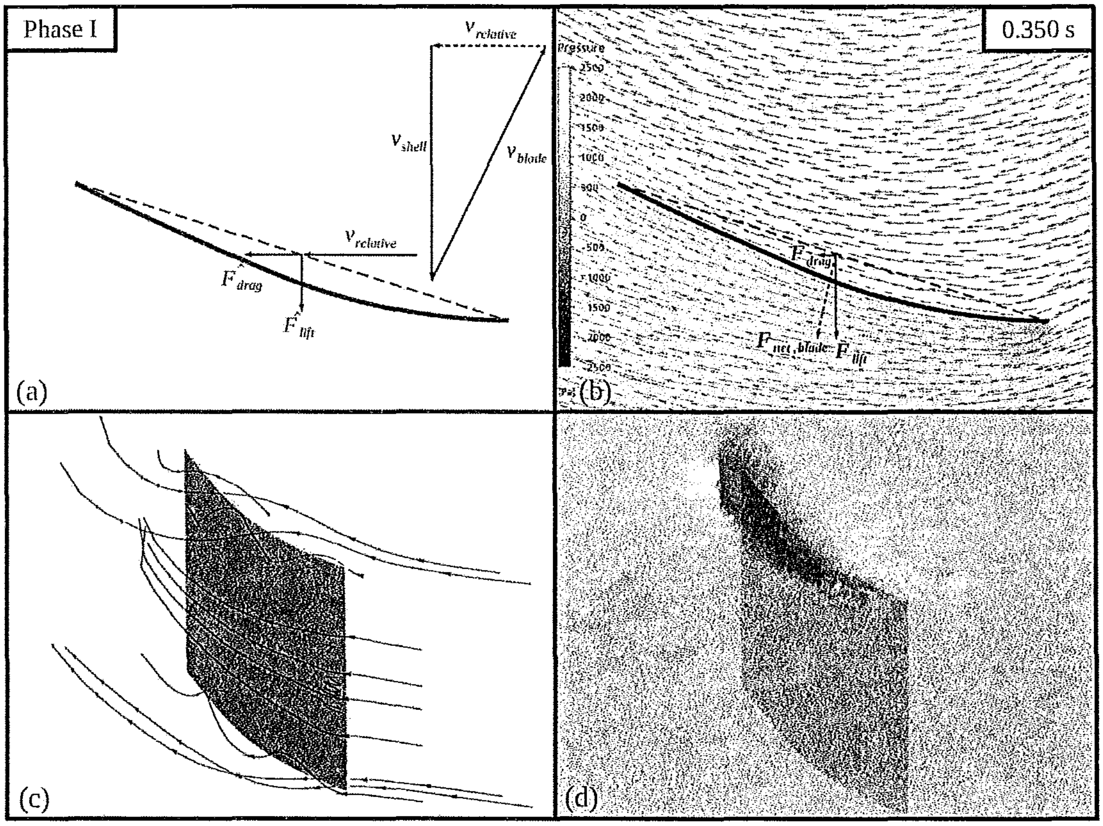

Figure 3.8: Flow characteristics for Phase I of the drive (at 0.35 s). (a) The shell is moving downward and the oar is rotating with a counter-clockwise angular velocity. Velocities and forces are as in Figure 1.3. (b) Pressure contour and velocity vectors of the flow for a plane slice through the middle of the blade. The net force on the blade, decomposed into drag and lift components, is indicated. (c) Streamlines highlighting important flow characteristics. (d) Contour of the free surface in the region surrounding the blade

3.4.2 Phase II

From 0.35 s to 0.40 s the blade is still moving laterally away from the shell, but now with negative slip (Figure 3.4). In this phase, $\alpha_{nominal}$ increases at a much quicker rate than in Phase I, rising from 25° to 45° in 0.05 s (Figure 3.9 a). The flow increasingly spills over the top edge of the blade, strengthening the horizontal vortices and resulting in a growing bulge in the free surface over and depression behind the blade (Figure 3.9 c, d). Flow over the bottom edge also increases with the rising $\alpha_{nominal}$. At 0.36 s there is a sudden rise in the pressure difference across the blade (~ 4 kPa), leading to a rapid increase in the propulsive force that is primarily lift-induced (Figure 3.9 b).

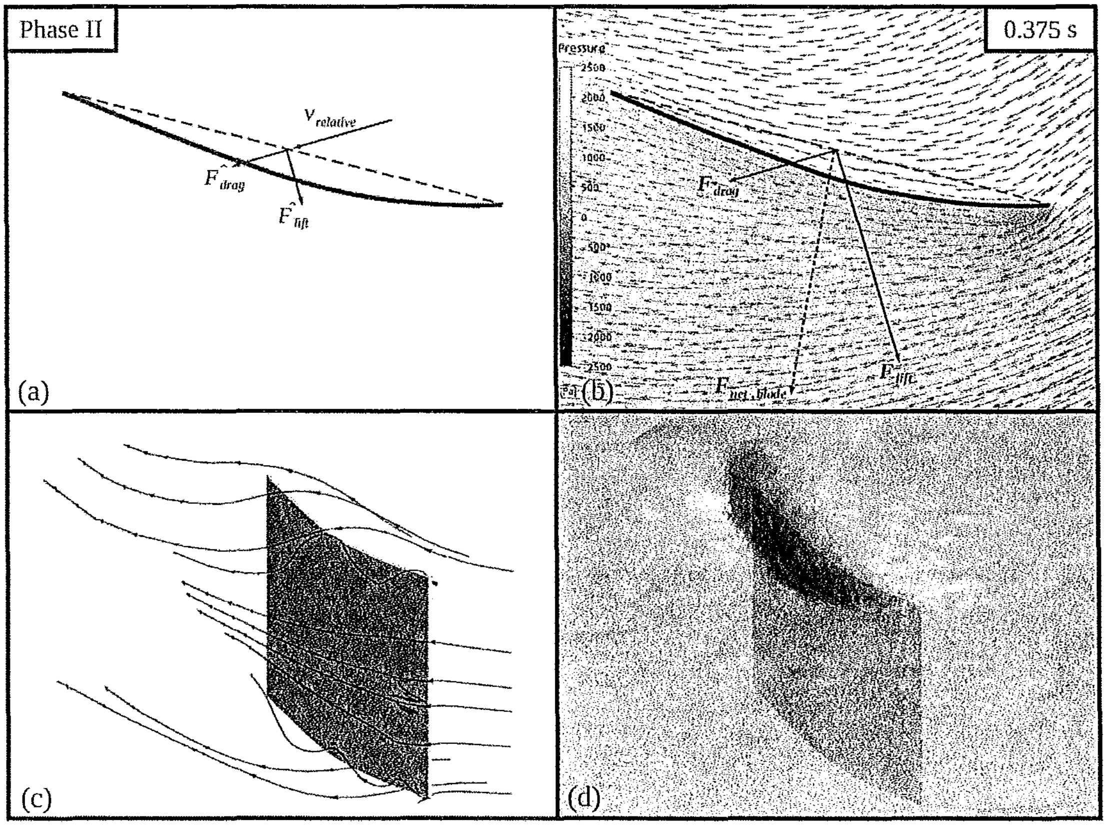

Figure 3.9: Flow characteristics for Phase II of the drive (at 0.375 s). (a) – (d) are as in Figure 3.8

The drag and lift forces continue to increase until 0.39 s, at which point the propulsive force reaches its maximum value (Figure 3.7). This is followed by a sharp drop in the propulsive force at 0.4 s, again largely due to the falling lift. The rapid increase in lift followed by a sharp decrease leads to the highest blade propulsive force during the stroke occurring in this phase.

The lift behaviour in this phase can be attributed to dynamic stall characteristics of the blade. Experiments on pitching airfoils with a rapidly increasing angle of attack reveal a similar increase in lift followed by a sharp decrease over a short period of time (Carr, 1988). As the incident flow on a rapidly pitching airfoil increases beyond the angle of attack for static stall (for a stationary airfoil, angle of attack where flow separation past the leading edge occurs, leading to large reduction in lift), a vortex develops at the leading edge. As this vortex grows and is convected downstream along the airfoil surface, its suction effect causes an increase in lift. When the vortex is eventually shed from the surface, the lift decreases sharply and the net force on the airfoil becomes primarily drag-induced. This phenomenon is caused by a time lag in the pressure response to the changing angle of attack, resulting in the airfoil experiencing a lower angle of attack than would be experienced under static conditions. Although these experiments were performed on high aspect ratio airfoils (primarily two-dimensional flow along the chord line), the effect that the formation and motion of vortices has on pressure changes for the low aspect ratio rowing blade can be drawn. The onset and growth of vortices, both horizontal and vertical, on the low-pressure (back) surface of the blade leads to a decreasing relative pressure there, resulting in a higher lift force. As vortices are shed, there is a rapid decrease in the relative pressure at the back of the blade, leading to an abrupt reduction in lift.

3.4.3 Phase III

From 0.4 s to 0.5 s, the blade continues to move laterally away from the shell, still with a negative slip (Figure 3.4). The nominal angle of attack continues to rapidly sweep across the blade, increasing from 45° to 85° (Figure 3.10 a). The rising $\alpha_{nominal}$ causes the vertical vortex near the blade tip to grow as the flow approaches the blade at a steeper incidence. By 0.45 s ($\alpha_{nominal} \approx 60°$), flow reversal is seen on most of the back surface of the blade, explaining the decreasing lift force during this phase (Figure 3.10 b). Flow over the top and bottom edges of the blade also increases as $\alpha_{nominal}$ approaches normal to the blade chord line, leading to growing horizontal vortices on the back of the blade (Figure 3.10 c). The strong horizontal vortices caused by spillover from the top and bottom surfaces maintain a high pressure difference across the blade (~2.5 kPa), causing the free surface bulge and depression to grow (Figure 3.10 d). These horizontal vortices, which are more pronounced toward the shaft side of the blade, and the persistence of the vertical vortex near the tip explain the rise in drag force during this phase. This increasing influence of drag maintains a high propulsive force during this phase (Figure 3.7).

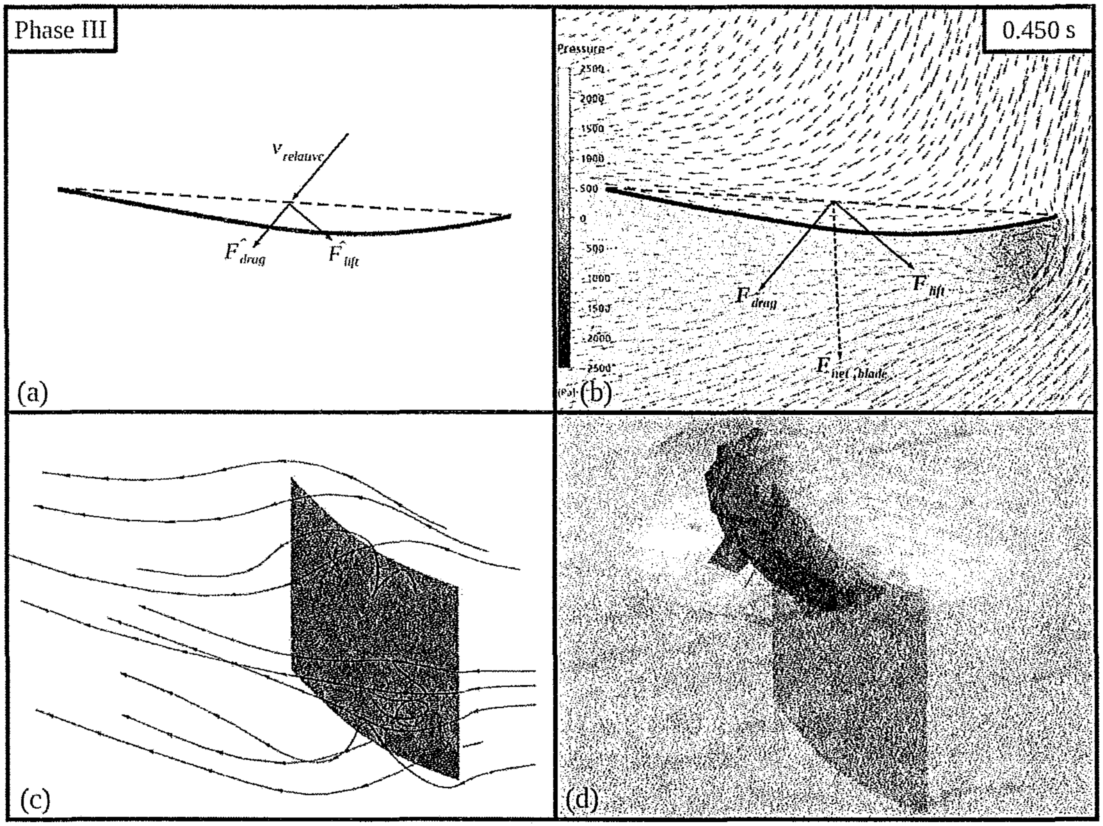

Figure 3.10: Flow characteristics for Phase III of the drive (at 0.45 s). (a) – (d) are as in Figure 3.8

3.4.4 Phase IV

After 0.50 s, the blade begins to move laterally back toward the shell, still with negative slip (Figure 3.4). The nominal angle of attack moves past perpendicular to the blade surface, making the shaft side the leading edge (Figure 3.11 a). The nominal angle of attack increases at its quickest rate, reaching 155° (25° as seen by the shaft side) by 0.60 s. With the aid of the persisting vertical vortex near the blade tip, the flow once again attaches to the back of the blade (Figure 3.11 b). The strength of this vertical vortex causes the flow behind the blade to converge near the tip where it meets the flow moving past the trailing edge from the front of the blade. The reattachment of the flow and the presence of the vertical vortex near the tip help to maintain a strong pressure difference across the blade (~ 2.5 kPa), leading to a slight rise in the lift force and a drop in the drag at 0.55 s. Flow over the top and bottom edges continues to increase during this phase, causing the horizontal vortices located at the top and bottom of the back surface to grow (Figure 3.11 c).

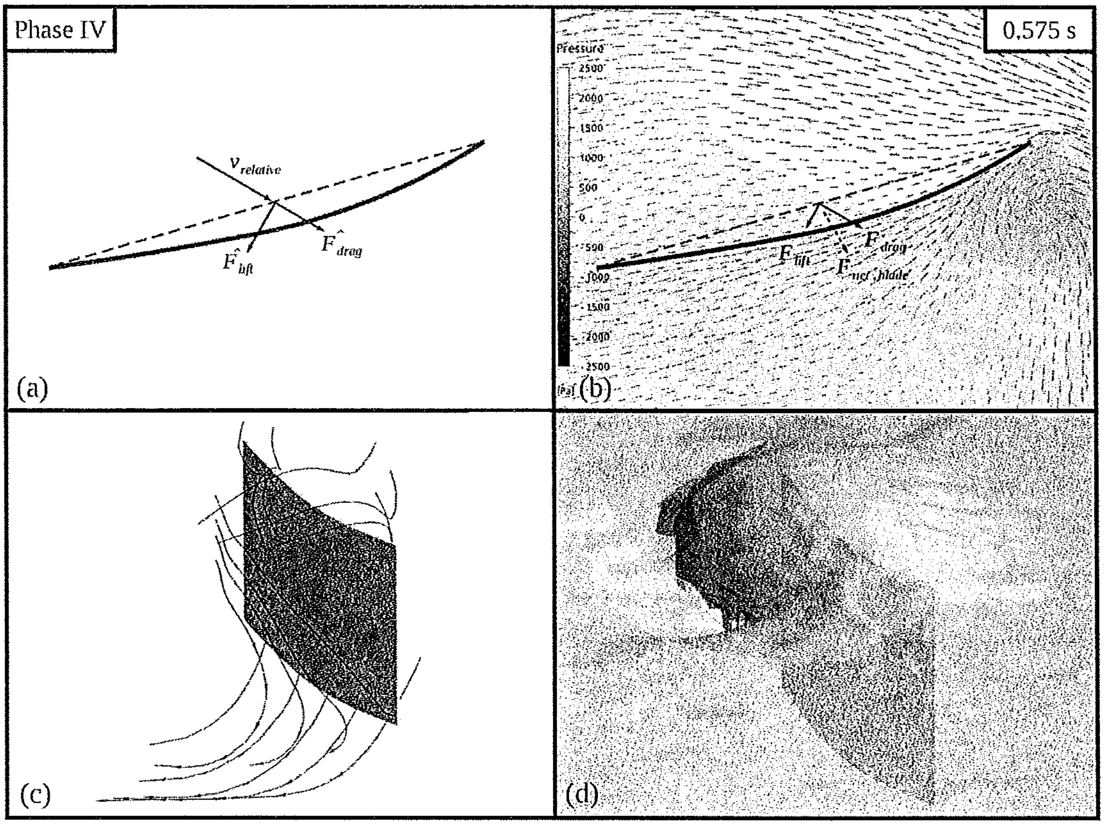

Figure 3.11: Flow characteristics for Phase IV of the drive (at 0.575 s). (a) – (d) are as in Figure 3.8

With the flow now approaching the blade from the shaft side, it stretches these vortices from the shaft side of the blade toward the tip. This is reflected in the bulge and depression of the free surface moving towards the tip (Figure 3.11 d). At 0.575 s, the vertical vortex at the tip sheds from the blade as the flow over the back surface of the blade increases. The shedding of this vortex explains the drop in pressure difference across the surface (down to ~ 1 kPa) which leads to a sharp decrease in $F_{Propulsive}$ by the end of this phase (Figure 3.7).

3.4.5 Phase V

Between 0.6 s and 0.65 s the blade continues to move laterally towards shell, and the slip becomes positive again (Figure 3.4). The nominal angle of attack continues to increase, reaching 180° by the end of the phase (Figure 3.12 a). The large horizontal vortex at the bottom of the blade detaches in this phase, causing the flow to further converge on the back surface of the blade near the tip, resulting in a high pressure region (~ 2 kPa) now occurring on this side near the shaft (Figure 3.12 b). This leads to a switch in direction of the pressure difference across the blade, causing negative drag and lift for the 0.05 s of this phase. The horizontal vortices caused by increasing flow over the top and bottom edges continue to strengthen as the flow approaches from an increasingly shallow $\alpha_{nominal}$ (seen from the shaft side of the blade). These vortices drag the horizontal streamlines vertically on the back of the blade as the flow moves toward the tip (Figure 3.12 c). This is accompanied by the surface bulge and depression also moving toward the tip (Figure 3.12 d). As the flow remains attached to the back of the blade, drag effects are minimal, and lift contributes primarily to the propulsive force. The reversed pressure difference in this phase causes the propulsive force vector to be directed opposite to the shell motion, acting to reduce shell velocity (Figure 3.7).

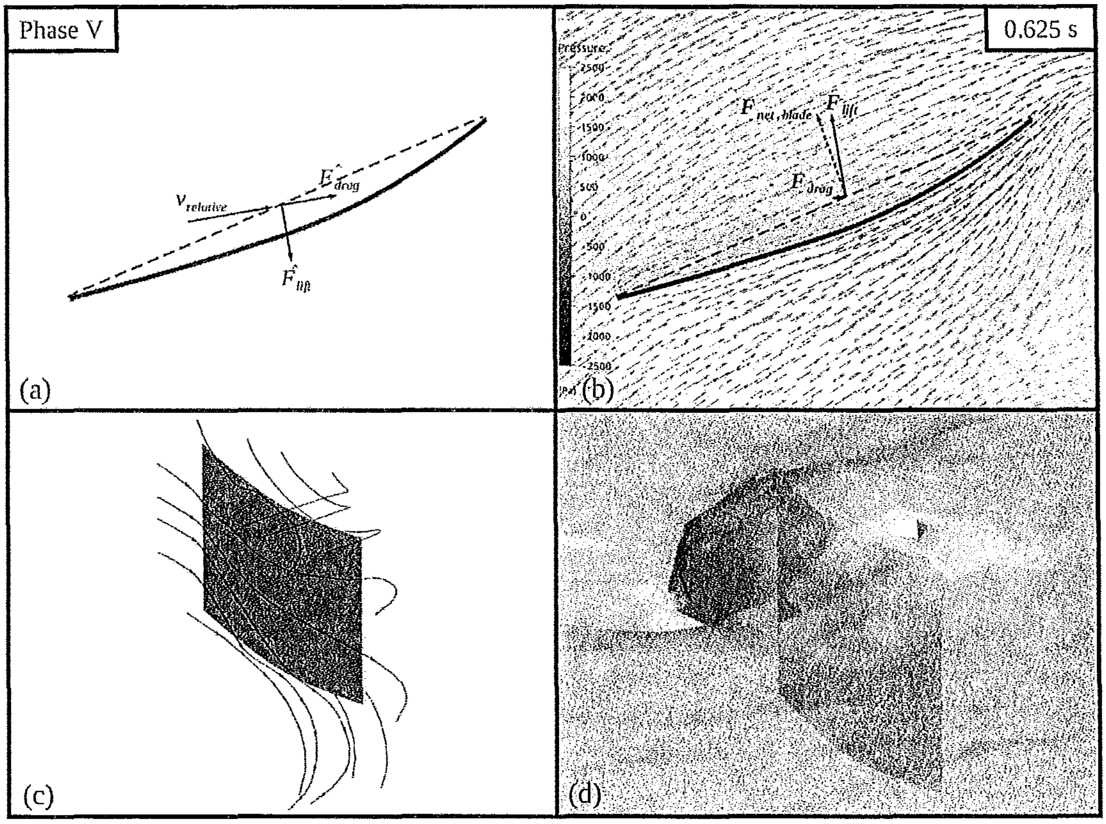

Figure 3.12: Flow characteristics for Phase V of the drive (at 0.625 s). (a) – (d) are as in Figure 3.8

3.4.6 Phase VI

During the final phase of the drive, (0.65 s to 0.74 s), the blade continues to move laterally towards the shell with a positive slip (Figure 3.4). The nominal angle of attack continues to increase, but at a much slower rate. Reaching 190° by the end of the drive, the flow becomes incident on the back surface of the blade (Figure 3.13 a).

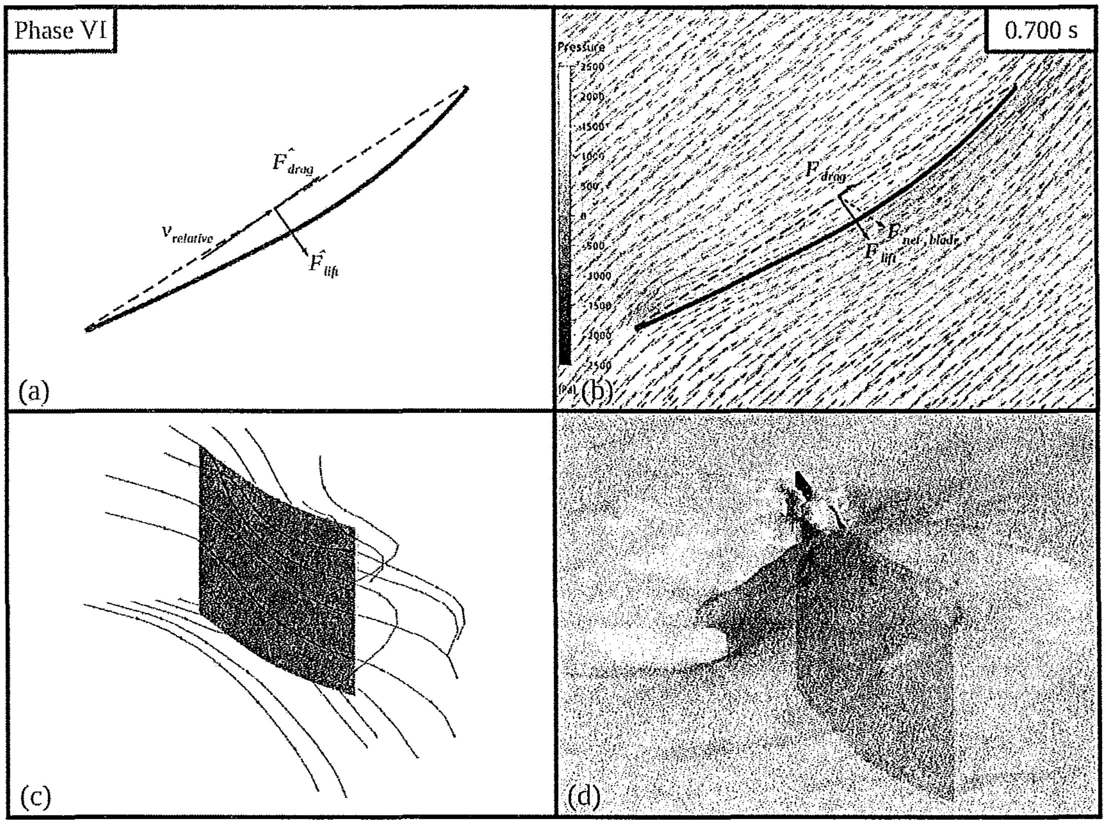

Figure 3.13: Flow characteristics for Phase VI of the drive (at 0.7 s). (a) – (d) are as in Figure 3.8

The flow stays attached on both sides of the blade, and the horizontal vortex near the top edge remains attached and continues to grow and move radially towards the blade tip (Figure 3.13 c), leading to a low relative pressure region (~ 2 kPa) at the back surface of the blade near the tip (Figure 3.13 b). Although $\alpha_{nominal}$ is incident on the back surface of the blade, the low pressure region on this side causes a high flow velocity across this surface. The shallow $\alpha_{nominal}$ causes the horizontal vortex present off of the back of the blade near the bottom edge to continue to move radially outward toward the tip and beyond. Correspondingly, the blade slides away from the created bulge and depression, and these surface conditions begin to dissipate (Figure 3.13 d). Drag and lift are once again positive, acting in the direction of the shell and aiding propulsion. Drag is low in this phase, similar to Phase I, owing to the shallow nominal angle of attack. The effect on the propulsive force is that it is low, but once again positive (Figure 3.7).

3.4.7 Summary of flow during a stroke

In short, the first half of the drive has been shown to generate primarily lift forces on the blade, as it moves through the water with a shallow but increasing angle of attack. This lift-induced propulsive force is small, but increases with the steeper flow incidence. Towards the middle of the drive dynamic stall behaviour on the blade is exhibited. As the angle of attack continues to increase, attached vortices are shed, explaining the rapid increase followed by a sharp decrease in lift, which in turn heavily influences the propulsive force. The middle of the stroke maintains a high propulsive force, increasingly influenced by drag, as the flow approaches the blade at a high angle of attack and is separated. Towards the end of the stroke, there is a period where the propulsive force acts opposite to the shell motion, effectively slowing the shell down. Finally, the end of the stroke is characterized by a low propulsive force, once again primarily lift-induced owing to a shallow angle of attack.

4 Conclusions and Future Work

4.1 Conclusions

Using numerical modelling, the previously unknown dynamic flow behaviour of a rowing oar blade in motion through a stroke has been simulated. Several intermediate steps were necessary, however, in order to achieve this end result. The steady-state experiments of a quarter-scale oar blade in a water flume (Caplan and Gardner, 2007b) were reproduced using a CFD simulation. A comparison of the simulated drag and lift coefficients to those from the experiments revealed a very good match, providing confidence in the numerical model, including its free surface and turbulence treatment, to handle similar flow conditions. These flow coefficients for the quarter-scale blade in a flume were then compared to the drag and lift coefficients for a simulated full-scale blade in open water conditions, again under steady conditions. Although the coefficients from both simulations followed the same trend, the full-scale blade coefficients were found to be between 20% and 30% lower that the quarter-scale blade. This variance was deemed due to both the different Reynolds number of the flows, and to the constraining effect that the flume walls had on the quarter-scale blade flow.

The next stage of analysis involved examining the unsteady behaviour of a blade in motion during a stroke, as it was suspected that this flow was substantially different than the steady-state flow case. This was achieved by the marriage of two models – a CFD model which enabled the dynamic flow around an oar blade during a stroke to be resolved, combined with an analytical rowing shell velocity model. The domain model was modified to allow for blade motion by adding a rotating domain nested within the larger stationary domain to simulate oar rotation. The complex interacting motion of a rowing shell, oars, and rowers was modelled using a force-based analysis of the interacting systems. This model accounted for the propulsive force created by the motion of the blade through the water, an analytical treatment of shell drag, and the momentum due to the motion of the crew with respect to the shell. With an input of oar angular velocity, and a modelled motion of the crew within the shell, a resultant shell velocity was generated. The ability of this model to replicate an experimentally obtained velocity profile of a rowing shell provides confidence in its overall ability to simulate the hydrodynamic characteristics associated with a rowing blade in motion.

Analysis of the simulated blade motion in the water through the drive, and of the temporal development of the blade forces reveals six distinct flow regimes, which are investigated in detail. By examining the instantaneous flow around the blade, relations between the blade propulsive, drag, and lift forces are revealed, showing analogous behaviour to an oscillating airfoil.

In short, this complete analysis has afforded the opportunity to deconstruct and analyze the highly unsteady flow around a rowing oar blade for the first time. Information gleaned from this body of work – and more so from the potential research that will stem from it – will be of great interest to oar blade manufacturers and rowing biomechanics researchers alike. Oar manufacturers can employ an improved understanding of blade flow to create blade shapes which maximize the transfer of power input from the rower during the stroke into shell propulsion. Rowing biomechanics researchers can use this information to optimize stroke mechanics, improving the rower's efficiency in transferring power into shell propulsion. Changes in blade shape ultimately leading to faster crews cannot, however, occur in isolation. An improved blade design must also be congruent with existing rowing technique, such that rowers can easily adapt to its introduction. Likewise, changes in the rowing stroke must also be acceptable given the rowing blade used. A multidisciplinary approach involving the collaboration between those designing rowing blades and those using them, then, will certainly reap benefits ultimately resulting in faster crews.

4.2 Future Work

The opportunities for further oar blade research based on this introductory body of work are seemingly endless. The development of a comprehensive hydrodynamic-based rowing model allows investigation of numerous aspects of rowing, and how they contribute to bottom-line shell velocity. By changing a given parameter in the model, its ultimate effect on shell velocity can be quickly and easily observed. Equipment design modifications can be incorporated into the model by changing the profile shape of the oar blade, or its cant angle in the water. Rigging aspects such as oar length, gearing ratio, and blade pitch angle can also be examined. Further modifications to the rowing model will feature a generalized oar angular velocity and crew motion profile, allowing the ability to study effects of different stroke rates. In addition, the relation between the oar angular velocity and motion of the crew can be modified, being mindful to biomechanical constraints, to optimize the rowing stroke itself.

It is clear that there is still much to be investigated and revealed within the broader field of rowing, most notably within the hydrodynamics of oar blades which until now has largely been unexplored. The tools are now in place to carry out this work, to broaden our understanding of the science behind rowing, and to apply it to create faster rowers.

BIBLIOGRAPHY

Atkinson, W. C. (2007). *Validating the ROWING model.* Retrieved November 19, 2008, from Rowing computer research (or: how rowing really works): http://www.atkinsopht.com/row/validate.htm

Bardina, J. E., Huang, P. G., & Coakley, T. J. (1997). *Turbulence modeling validation, testing, and development.* NASA Technical Memorandum 110446, NASA.

Barre, S., & Kobus, J.-M. (1998). New facilities for measurement and modelling of hydrodynamic loads on oar blades. In S. J. Haake (Ed.), *The Engineering of Sport: Design and Development* (pp. 251-260). Blackwell Science Ltd.

Baudouin, A., & Hawkins, D. (2002). A biomechanical review of factors affecting rowing performance. *British Journal of Sports Medicine , 36*, 396-402.

Brackbill, J. U., Kothe, D. B., & Zemach, C. (1992). A continuum method for modelling surface tension. *Journal of Computational Physics , 100* (2), 335-354.

Brearley, M. N., de Mestre, N. J., & Watson, D. R. (1998). Modelling the rowing stroke in racing shells. *The Mathematical Gazette , 82* (495), 389-404.

Cabrera, D., Ruina, A., & Kleshnev, V. (2006). A simple 1+ dimensional model of rowing mimics observed forces and motions. *Human Movement Science , 25*, 192-220.

Caplan, N., & Gardner, T. N. (2007). A mathematical model of the oar blade-water interaction in rowing. *Journal of Sports Sciences , 25* (9), 1025-1034.

Caplan, N., & Gardner, T. N. (2007). Optimization of oar blade design for improved performance in rowing. *Journal of Sports Sciences , 25* (13), 1471-1478.

Carr, L. W. (1988). Progress in analysis and prediction of dynamic stall. *Journal of Aircraft , 25* (1), 6-17.

Concept2. (2007). *Oar testing.* Retrieved November 18, 2007, from Concept2: http://www.concept2.com/us/oars/pursuit/oar_testing.asp

Coppel, A., Gardner, T., Caplan, N., & Hargreaves, D. (2008). Numerical modelling of the flow around rowing oar blades. In M. Estivalet, & P. Brisson, *The Engineering of Sport 7* (pp. 353-361). Paris: Springer.

Crew terminology. (2002). Retrieved September 24, 2009, from History of collegiate crew in connecticut: http://www.fhiplan.com/ctrowing/crewterms.htm

Ekaterinas, J. A., & Menter, F. R. (1994). Computation of oscillating airfoil flows with one- and two-equation turbulence models. *AIAA Journal , 32* (12), 2395-2365.

Gueyffier, D., Li, J., Nadim, A., Scardovelli, R., & Zaleski, S. (1999). Volume-of-fluid interface tracking with smoothed surface stress methods for three-dimensional flows. *Journal of Computational Physics , 152*, 423-456.

Hirt, C. W., & Nichols, B. D. (1981). Volume of fluid (VOF) method for the dynamics of free boundaries. *Journal of Computational Physics , 39*, 201-225.

International Towing Tank Conference. (2002). ITTC - Recommended Procedures. *Proceedings of the 23rd ITTC 2002.*

Jones, W. P., & Launder, B. E. (1972). The prediction of laminarization with a two-equation model of turbulence. *International Journal of Heat and Mass Transfer , 15* (2), 301-314.

Kleshnev, V. (2007, December). *Rowing Biomechanics Newsletter , 7* (81).

Kleshnev, V. (1999). Propulsive efficiency of rowing. *Proceedings of the XVII International Symposium on Biomechanics in Sport* (pp. 224-228). Perth: Edith Cowan University.

Macrossan, M. N. (2008). *The direction of water force on a rowing blade and its effect on efficiency.* Mechanical Engineering Report No. 2008/03, University of Queensland.

McCroskey, W. J. (1982). Unsteady airfoils. *Annual Review of Fluid Mechanics , 14*, 285-311.

McMahon, T. A. (1971). Rowing: a simlarity analysis. *Science , 173* (3994), 349-351.

Menter, F. R. (1992). Influence of freestream values on k-omega turbulence model predictions. *AIAA Journal , 30* (6), 1657-1659.

Menter, F. R. (1994). Two-equation eddy-viscosity turbulence models for engineering applications. *AIAA Journal*, *32* (8), 1598-1605.

Menter, F. R., Kuntz, M., & Langtry, R. (2003). Ten years of industrial experience with the SST turbulence model. In K. Hanjalic, Y. Nagano, & M. Tummers (Ed.), *Turbulence, Heat and Mass Transfer 4.* Begell House, Inc.

Millward, A. (1987). A study of the forces exerted by an oarsman and the effect on boat speed. *Journal of Sports Sciences*, *5*, 93-103.

Nolte, V. (1993, July/August). Do you need hatchets to chop your water? *American Rowing*, pp. 23-26.

Nolte, V. (2009). Shorter oars are more effective. *Journal of Applied Biomechanics*.

Pope, D. L. (1973). On the dynamics of men and boats and oars. In J. L. Bleustein, *Mechanics and Sport* (pp. 113-130). New York: AMSE.

Simpson, R. L. (1996). Aspects of turbulent boundary-layer separation. *Progress in Aerospace Sciences*, *32*, 457-521.

Wellicome, J. F. (1967). Some hydrodynamic aspects of rowing. In J. G. Williams, & A. C. Scott, *Rowing: A Scientific Approach* (pp. 22-63). London: Kaye & Ward Ltd.

Wilcox, D. C. (1988). Reassessment of the scale-determining equation for advanced turbulence models. *AIAA Journal*, *26* (11), 1299-1310.

Williams, J. G. (1967). Rowing - art or science? In J. G. Williams, & A. C. Scott, *Rowing: A Scientific Approach* (pp. 20-21). London: Kaye & Ward Ltd.

Zwart, P. J., Godin, G. G., Penrose, J., & Rhee, S. H. (2008). Simulation of unsteady free-surface flow around a ship hull using a fully coupled multi-phase flow method. *Journal of Marine Science and Technology*, *13*, 346-355.